A Persistent Deep Anticyclonic Vortex in the Rockall Trough Sustained by Anticyclonic Vortices Shed From the Slope Current and Wintertime Convection

Angelina Smilenova[1,2], Jonathan Gula[3], Mathieu Le Corre[3], Loïc Houpert[4], and Yves Reecht[5]

[1]Earth and Ocean Sciences, School of Natural Sciences, National University of Ireland, Galway (NUIG), University Road, Galway, Ireland, [2]Oceanographic Services, Marine Institute, Galway, Ireland, [3]University of Brest, CNRS, IRD, Ifremer, Laboratoire d'Océanographie Physique et Spatiale (LOPS), IUEM, Brest, France, [4]National Oceanography Centre (NOC), Southampton, UK, [5]Institute of Marine Research, Bergen, Norway

Abstract The presence of a persistent surface anticyclone centered at approximately 55°N, 12°W in the Rockall Trough, northeast North Atlantic, has been previously noted in satellite altimetry data. Here, we show that this surface anticyclone is the imprint of a deep, persistent, non-stationary anticyclonic vortex. Using wintertime 2007 and 2011 ship-board data, we describe the anticyclone's vertical structure for the first time and find that the anticyclone core is partly made of warm and salty Mediterranean Overflow Water. The anticyclone has a radius of ~40 km, it stretches down to 2,000 m, with a velocity maximum around 500 m. To analyze the anticyclone's generating mechanism, we use a mesoscale-resolving (~2 km) simulation, which produces a realistic pattern of the Rockall Trough anticyclone. The simulation indicates that the anticyclone is locally formed and sustained by two types of processes: wintertime convection and merger with anticyclonic vortices shed from the slope current flowing poleward along the eastern Rockall Trough slope. Intense negative vorticity filaments are generated along the Rockall Trough south-eastern slope, and they encapsulate Mediterranean Overflow Water as they detach and grow into anticyclonic vortices. These Mediterranean Overflow Water-rich vortices are advected into the trough, consequently merging with the Rockall Trough anticyclone and sustaining it. We suggest that the Rockall Trough anticyclone impacts regional intermediate water masses modifications, heat and salt budgets locally, and further afield into the neighboring subpolar northeast North Atlantic.

Plain Language Summary Water masses of different origins converge in the Rockall Trough, a deep bathymetric depression in the northeast North Atlantic, and undergo transformations with direct implications for the inflow of warm water into the Nordic Seas. We use in situ observations to document, for the first time, the vertical structure of a subsurface anticyclone, which is a clockwise oceanic vortex in the trough. We show that the anticyclone has a radius of ~40 km, extends down to 2,000 m, with a velocity maximum at 500 m depth. Its core is made of warm and salty Mediterranean water. We use outputs from a high-resolution (~2 km) realistic simulation to study the mechanisms driving the anticyclone. We show that the anticyclone is impacted predominantly by two different processes. One is the wintertime convection, which mixes waters from the surface down to 1,000 m inside the anticyclone. The other is the merger with smaller vortices that pinch off the slope current flowing northward along the Porcupine Bank, south of the Rockall Trough, and feed the anticyclone with water masses of Mediterranean origin. We showcase the potential impact of the anticyclone on the regional and nearby northeast North Atlantic heat and salt distributions.

1. Introduction

Eddies at the mesoscale (Chelton et al., 2007) and the submesoscale (McWilliams, 1985) populate the ocean. Mesoscale eddies are usually defined by a radius larger or equal to the first Rossby deformation radius, which has an inverse relationship with latitude and varies between 40 km at midlatitudes to about 10 km at 60°N (Chelton et al., 1998). (Sub)mesoscale eddies are three-dimensional oceanic structures, found at various depths within the water column (e.g., Bosse et al., 2016; Ebbesmeyer et al., 1986). They are common in

the deep ocean (Petersen et al., 2013), where they partake in deep and intermediate water masses dynamics (Bosse et al., 2016). Depending on the depth of intensification, eddies are categorized as surface-intensified or subsurface-intensified (Assassi et al., 2016). Their generating mechanisms range from large-scale currents instabilities to small-scale turbulence or deep convection events (e.g., Carton, 2001; McWilliams, 1985). The eddy's dynamics is profoundly nonlinear and drives energy fluxes between scales. Eddies can extract or provide momentum and energy to the large-scale mean currents, thus modifying the overall large-scale ocean circulation (e.g., Le Corre et al., 2020; Lozier, 1997; Morrow & Birol, 2004).

The importance of mesoscale eddies on the large-scale circulation, (e.g., Chelton et al., 2007; Zhao, Bower, Yang, & Lin, 2018; Zhao, Bower, Yang, Lin, & Zhou, 2018) and their role in the formation and redistribution of large-scale thermohaline properties and tracers are well established (e.g., Bashmachnikov et al., 2018; Frenger et al., 2018; Testor et al., 2018; Treguier et al., 2012). Water masses trapped within eddies' cores can retain their thermohaline properties while being transported unobtrusively away from their place of origin (e.g., Flierl, 1981; Zhang et al., 2014). Overall, eddies account for about 50% of the world's ocean circulation variability (Chelton et al., 2007), impacting both zonal and meridional circulation patterns at intermediate and deeper levels (Demirov & Pinardi, 2007). In the subpolar northeast North Atlantic (NA), the presence or absence of eddies significantly impacts meridional velocities and consequently the total poleward heat transport variability on subseasonal to interannual timescales (Houpert et al., 2018; Zhao, Bower, Yang, & Lin, 2018).

Investigations of vortices, propagating or topographically trapped, are thus of importance, as they form a fundamental part of the large-scale and regional circulation, and consequent heat, salt, and nutrients transports. Here, we investigate a subsurface anticyclone in the Rockall Trough (RT) and showcase that locally generated (sub)mesoscale eddies hold the potential to impact the large-scale dynamics of the northeast NA.

The RT basin (Figure 1), northeast NA, is a deep bathymetric depression, elongating northeast from the Porcupine Abyssal Plain in the south to the Wyville Thomson Ridge in the north. The trough consists of numerous deep subbasins, segregated by basement ridges (Naylor et al., 1999), shaping a complex regional bottom topography.

The southern RT is in close proximity to the NA subtropical and subpolar gyres boundaries, making the region a key area of interplay between upper and intermediate water masses of both subtropical (Eastern North Atlantic Central Water [ENACW] and Mediterranean Overflow Water [MOW]) and subpolar (Sub-Arctic Intermediate Water [SAIW] and Labrador Sea Water [LSW]) origins (Figure 1). ENACW is the lightest of the four water masses, falling within the 26.85–27.2 kg m^{-3} density range (Mosquera Giménez et al., 2019), underlined by SAIW, settled along 27.27–27.3 kg m^{-3} isopycnals (Wade et al., 1997). MOW occupies the 27.38–27.72 kg m^{-3} isopycnals (Mosquera Giménez et al., 2019), which overlies the LSW, spreading within the 27.74–27.82 kg m^{-3} isopycnals (Courtois et al., 2020; Garcia-Quintana et al., 2019). At the RT southern approach, subpolar SAIW and LSW and subtropical ENACW and MOW water masses enter the channel along their respective westward and eastward pathways (Figures 1a, 1c, and 1d). As the channel narrows and waters continue northward into the trough, interactions between the different water masses become apparent, with evidence of interior mixing within the central RT, as depicted in the WOA18-based southern and central RT T/S diagrams (Figure 1b). Thermohaline properties in the central RT are more homogenous in comparison with thermohaline properties at the entrance of the trough or the neighboring subpolar NA waters (Figures 1e and 1f).

A pronounced mesoscale eddy activity in the subpolar northeast NA, particularly the RT region, has been highlighted by satellite-based studies (e.g., Heywood et al., 1994; Volkov, 2005; White & Heywood, 1995). The notable RT mesoscale activity is thought to be influenced by the northward flowing (sub)branches of the North Atlantic Current (NAC) (Xu et al., 2015). The RT region is additionally impacted by the presence, strength, and seasonality of the poleward flowing, topography steered, deep core continental slope current (Graham et al., 2018; Marsh et al., 2017). The RT deep subsurface mesoscale activity is illustrated in few observation and model-based studies. At depth, mesoscale activity can be evaluated using eddy available potential energy (EAPE), which measures the energy stored in vertical isopycnal displacements (Lorenz, 1955; Roullet et al., 2014). In the Argo-based atlas of Roullet et al. (2014), a deep subsurface EAPE maximum of approximately 0.1 m^2 s^{-2} at 1,000 m depth is visible in the central RT (their
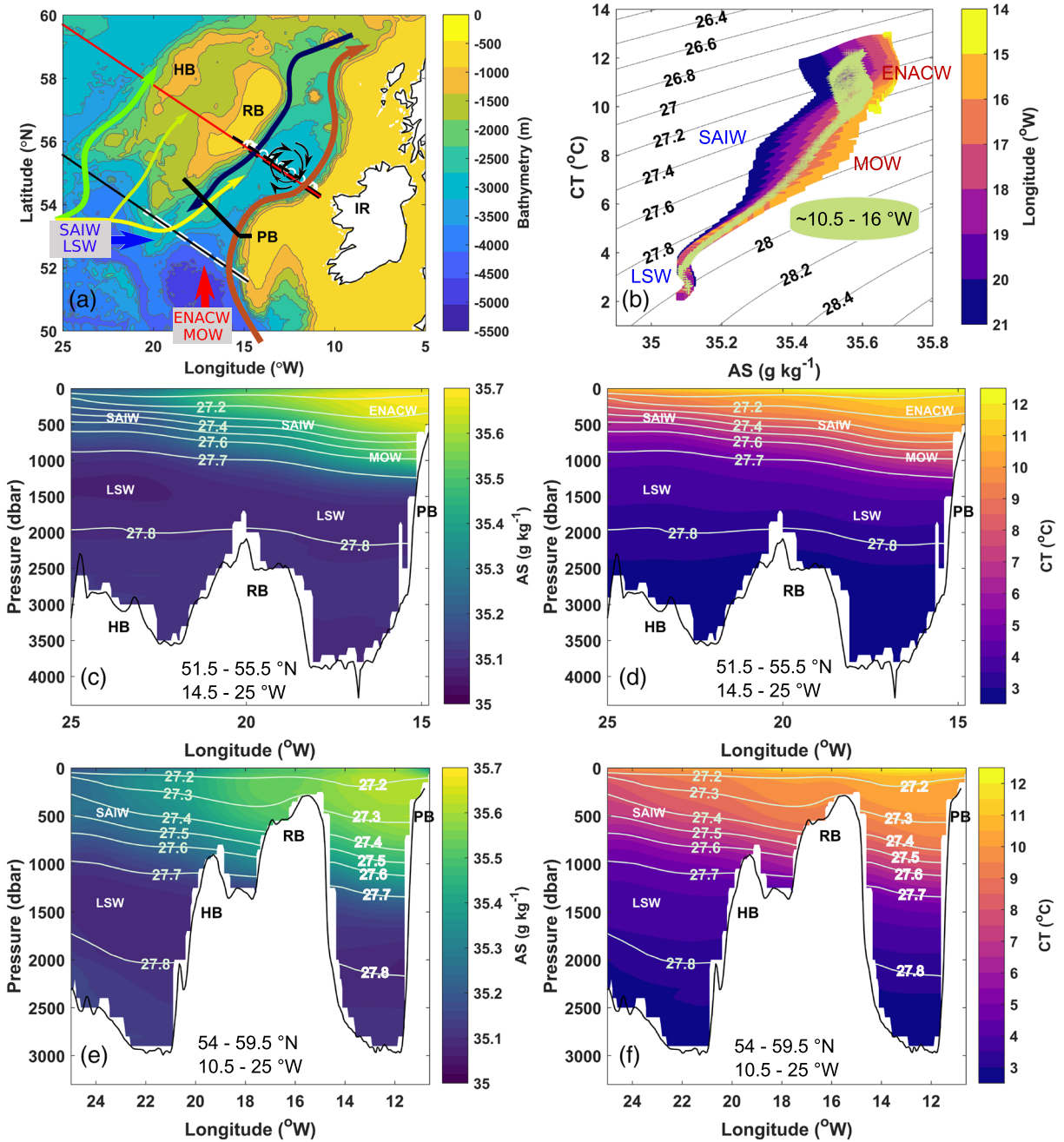
Figure 1. (a) Study area bathymetry map (500 m level-step) with survey transect line (~54–56°N) stations (white circles); thick black lines showing ship-board data used in section 2.3.2. In (b) yellow to purple T/S diagram represents waters at the southern Rockall Trough (RT) approach, along the southern black-white dashed line (~14.5–21°W, WOA18); data are displayed as a function of longitude. Light green T/S diagram in (b) represents waters within the central RT, along the black-red line (~10.5–16°W, WOA18). Averaged 2005–2017 absolute salinity (AS) (g kg^{-1}) and conservative temperature (CT) (°C) fields along the thin black WOA18 transect line are presented in (c) and (d), respectively. Averaged 2005–2017 AS and CT vertical distributions along the red WOA18 transect line are shown in (e) and (f), respectively. In (a) currents' pathways in the area (after Holliday et al., 2015) are represented by colored arrows, where yellow to green pathways represent North Atlantic current (NAC) (sub)branches; orange and dark blue arrows represent the slope current and Wyville Thomson Overflow Water (WTOW) pathways, respectively. The black curved arrows, turning clockwise, locate the presence of a surface anticyclonic circulation in the central RT, first noted in Ellett et al. (1986). Letter annotations: IR, Ireland; HB, Hatton Bank; RB, Rockall Bank; PB, Porcupine Bank.
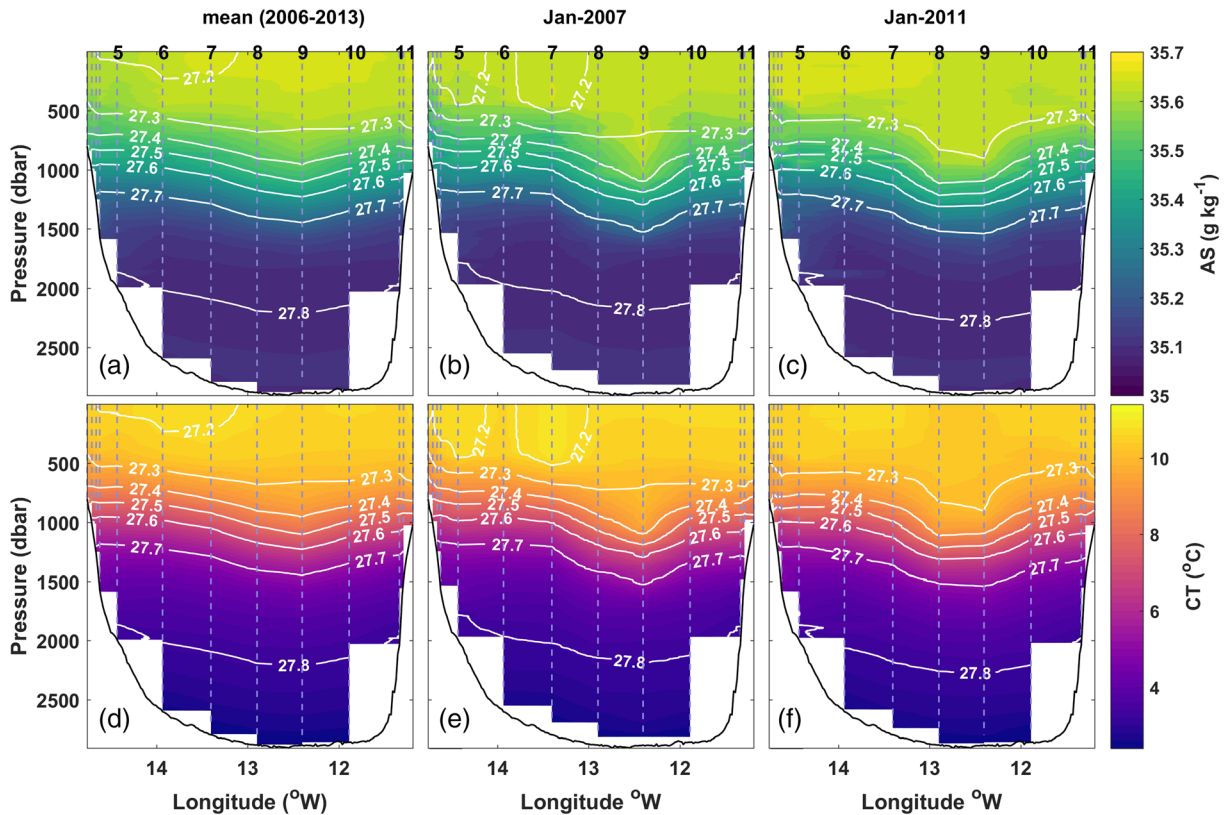
Figure 2. (top) Longitude-pressure in situ-derived absolute salinity (AS) (g kg^{-1}) and (bottom) conservative temperature CT (°C) (a, d) averaged over the 2006–2013 period, and for (b, d) January 2007, and (c, e) January 2011. Light gray dashed lines in all plots are representative of stations locations. Dark gray lines show potential density (σ_θ) (kg m^{-3}), referenced to 0 dbar.

Figure 2d). The same hotspot of EAPE is more pronounced in Vic et al. (2018) (their Figure 2b), where an updated version of Roullet et al. (2014) database is used. Interestingly, this EAPE maximum is not reproduced by their numerical model (which uses a dx ≈ 6 km resolution). An intense deep mesoscale activity in the central RT is also visible in Fischer et al. (2018), from the Argo-based eddy kinetic energy distribution at 1,000–1,500 m depth (their Figure 3b).

A surface, semipermanent anticyclone, centered at 55°N, 12°W, was identified by Xu et al. (2015) based on 20 years of altimetry data (their Figure 5). The presence of an anticyclone at 55°N, 12°W, at depth, was briefly noted in an earlier regional northeastern NA model-based study, exploring the origin and pathways of saline inflow through the RT and into the Nordic Seas (New et al., 2001).

Our inspection of wintertime ship-board Conductivity-Temperature-Depth (CTD) data, collected over the 2006–2013 period along a 54–56°N transect line (Figure 1a) within the central RT, reveals the presence of an intermediate water depth vortex, positioned at ~55.1°N, 12.6°W in January 2007 and January 2011. The subsurface-intensified anticyclone is also evident in the January 2012 temperature and salinity anomalies vertical distributions (supporting information Figure S1), however only partially, due to incomplete transect sampling. The collocation of the subsurface-intensified anticyclonic vortices detected in the transect ship-board data and the semipermanent surface anticyclonic signature, described in Xu et al. (2015) satellite-based study, prompted curiosity for investigations as to (1) whether the surface anticyclone is a manifestation of the subsurface-intensified anticyclone, (2) how this anticyclone is formed, and (3) how it could influence water masses in the region.

The paper is organized as follows: the observational data, model setup, and methods are presented in section 2. In section 3, we use the 2007 and 2011 eddy-opportunistic ship-board CTD data to describe the vertical structure of the subsurface-intensified anticyclone and confirm its relation with the surface anticyclone observed using satellite altimetry data. In section 4, we use high-resolution (~2 km) numerical simulations

and model-based Lagrangian experiments to investigate the origin of the anticyclone's water masses and its dynamics. Discussion and conclusions are presented in section 5.

2. Data Sets and Methods

2.1. Observational Data

2.1.1. Ship-Board Data

CTD data used here are, to our knowledge, the only repeated high vertical resolution (~1 m) ship-board measurements across the RT anticyclone. The CTD data have been collected during multidisciplinary wintertime surveys (Marine Institute, Ireland). Surveys were conducted in January–February months, between 2006 and 2013 along a ~54–56°N transect line (Figure 1a). Individual survey periods are as follows: 2006 (26 January to 2 February), 2007 (24 January to 2 February), 2008 (no survey), 2009 (5 February to 15 February), 2010 (5 February to 17 February), 2011 (3 January to 12 January), 2012 (3 January to 12 January, partial transect survey), and 2013 (5 January to 20 January, partial transect survey). Data were acquired using a Sea-Bird 9/11 plus CTD probe, with sampling rate of 24 Hz and temperature and conductivity accuracies of $\pm0.001°C$ and ±0.0003 S m^{-1} respectively. Independent temperature and salinity calibrations have been performed on discrete water samples using Sea-Bird SBE-35 digital thermometer and a Guildline Portasal salinometer (Model 8410A), respectively (McGrath et al., 2012). Additional surveys and data details are provided in Tables S1 and S2. Preliminary data processing has been performed with Seabird SBE software. Prior to analysis, all downcast data have been averaged to 1 m bins, compiled into a three-dimensional data array format: pressure/depth, station (latitude/longitude), and time (year), that is, [min:max pressure] × [number of stations] × [number of years]. Following Marnela et al. (2016), we linearly interpolated downcast data at 1 m interval to eliminate gaps in the vertical, with upper cast missing values extrapolated to the surface using uppermost cast observation as a constant value; no instabilities were removed or smoothed.

To derive estimates of water masses fractions within the RT anticyclone (section 2.3.2), we also used wintertime ship-board data, collected along another ~53–54/55°N transect line (Figure 1a), as part of the multidisciplinary surveys described above.

2.1.2. Satellite Altimetry

We use delayed-mode absolute dynamic topography (ADT) altimetry data, coinciding with the ship survey sampling, to explore the possible signature of the deep anticyclone at the surface. ADT data are produced by SSALTO/DUACS (Data Unification and Altimeter Combination System), processed and distributed by the Copernicus Marine and Environment Monitoring Service (CMEMS), and available online (http://www.marine.copernisuis.eu). We apply a simple eddy detection algorithm, outlined in section 2.3.3. Similarly to Halo, Backeberg, et al. (2014), Halo, Penven, et al. (2014), and Laxenaire et al. (2018), we use objectively mapped ADT, which represents the sum of sea level anomaly and mean dynamic topography, both referenced to over 20 year time-period in the Ssalto/Duacs 2014 ADT data set (Laxenaire et al., 2018; Pujol et al., 2016).

2.2. Model Output Data

We use the Coastal and Regional Ocean COmmunity (CROCO) model (Debreu et al., 2012), a variation of the Regional Oceanic Modeling System (ROMS) model (Shchepetkin & McWilliams, 2005). CROCO is a free-surface, terrain-following coordinate model, which solves the hydrostatic primitive equations for the velocity, potential temperature, and salinity with a seawater equation of state (Shchepetkin & McWilliams, 2005). CROCO is suitable for both basin-scale (O [10 km]) and nearshore (O [10 m]) processes modeling (Marchesiello et al., 2015; Penven et al., 2006).

2.2.1. Model Setup

We use outputs from a regional configuration covering the subpolar gyre, which has been described in Le Corre et al. (2020). The grid-space is dx ≈ 2 km and the simulation spans the 2002–2011 period. This grid resolves mesoscale eddies in all of the area and allows for the larger submesoscale eddies in some parts of the area.

A one way nesting approach is used, where two successive horizontal parent and child grids are defined, with respective resolutions of dx ≈ 6 km and dx ≈ 2 km. All domain bathymetry is derived from SRTM30 Plus (http://topex.ucsd.edu/WWW_htms/srtm30_plus.html) based on Sandwell and Smith (1997) 1-min resolution data set and incorporating higher resolution where available. A Gaussian smoothing kernel,

four times the topographic grid spacing, is used to avoid aliasing and achieve topographic smoothness at the grid scale. To avoid possible artifact pressure gradient errors in shallow regions with steep topography, local bottom topography smoothing is applied where steepness of topography exceeds a factor $r = 0.2$. Simple Ocean Data Assimilation (SODA; Carton & Giese, 2008) on 1 January 1999 is used to initialize the largest domain. The spin-up period is 2 years, using monthly averaged lateral SODA boundary conditions. Daily ERA-INTERIM fields provide the surface forcing for the parent grid, 12 hr ERA-INTERIM fields are used for the child grid. The parent grid has $1,152 \times 1,059$ points with 6–7 km resolution, as in Renault et al. (2016). This domain is subjected to a 3-year spin-up, and then daily fields are extracted during 8 years to create boundary conditions for the nest. The nested grid has $2,000 \times 1,600$ points, with a 2 km horizontal resolution. The Atlantic and subpolar gyre nests have 50 and 80 vertical levels, respectively. Vertical levels at the surface and the bottom are stretched to provide a better presentation of the top surface layer and flow-bottom topography interactions. Vertical mixing of momentum and tracers is parameterized with a k-ε model (GLS, Umlauf & Burchard, 2003). Bottom friction effect is parameterized through logarithmic law of wall with roughness length of 0.01 m.

2.2.2. Model Validations

The model does not assimilate observations and thus is not supposed to reproduce a specific observed mesoscale feature at any given time. However, we expect it to be able to reproduce a statistically similar large-scale circulation and mesoscale eddying activity. Below, we present comparisons of the mean hydrography and mesoscale activity between the model and observations.

The mean absolute salinity (AS), conservative temperature (CT), and potential density (σ_θ) in the model are compared to observation and reanalysis data sets along the RT section in Figure S2. We plot the last 2 years of the simulation (2010–2011), as they correspond to the period of the Lagrangian experiments (sections 4.2.2 and 4.3). Data sets include WOA18 (2005–2017), ISAS15 (2002–2015) (Gaillard et al., 2016; Kolodziejczyk et al., 2017), the SODA reanalysis (2010–2011) (used as initial and lateral boundary conditions for the North-Atlantic nest), the model (2010–2011), and the CTD data (2006–2013). Model data and observations are generally in quite good agreement. A remarkably similar and strong signature of the RT anticyclone is visible in both the CTD and the model data. The other climatological data sets cannot clearly resolve the structure of the RT anticyclone, possibly due to a lack of in situ data.

The representation of the mesoscale activity in the simulation can be evaluated through the EAPE. The modeled EAPE at 1,000 m matches well with the Argo-based EAPE at 1,000 m (Roullet et al., 2014) (Figure S3). In the central RT, both model and observations show a local maximum with comparable amplitude, related to the presence and nonstationarity of the RT anticyclone.

The above comparisons provide a good assessment that we can use the simulation to investigate the dynamics of the RT anticyclone and proceed to a Lagrangian analysis of water masses.

2.3. Methods

2.3.1. Subsurface Anticyclone Identification in In Situ Data

Subsurface-intensified anticyclones imprint the hydrographic field by isopycnal displacements, with doming of upper isopycnals and downward curving of lower layers isopycnals (Assassi et al., 2016; Barceló-Llull et al., 2017; McWilliams, 1985). Subsurface anticyclones are further characterized by low potential vorticity (PV) with respect to their ambient surroundings (D'Asaro, 1988; Gula et al., 2019; McWilliams, 1985; Molemaker et al., 2015). The anticyclonic vortex center can be defined as the location of the most extreme negative PV anomaly (Morel & McWilliams, 1997a). By visually inspecting AS, CT, σ_θ, and PV anomalies, we pinpoint the core's center to be where the highest or lowest values of all property anomalies overlap. The anticyclone's radius is then defined as the distance from the allocated core's center to the point where salinity and temperature anomalies drop to 0.025 g kg^{-1} and 0.25°C respectively, and density and PV anomalies climb up to 0.025 kg m^{-3} and down to -0.2×10^{-10} m^{-1} s^{-1}. The polarity and vorticity amplitude of the anticyclone are characterized using CTD-derived geostrophic velocities (GV) estimations. AS (g kg^{-1}), CT (°C), σ_θ (kg m^{-3}), and PV (m^{-1} s^{-1}) anomalies are calculated relative to mean values for 2006, 2009, 2010, and 2013, representing the undisturbed background; σ_θ is referenced to 0 dbar. PV anomalies calculations are based on the stretching term of Ertel PV (Q_{str}), derivation outlined in section 2.3.4. To convert the data to AS and CT, we use the TEOS-10 software (IOC, SCOR, and IAPSO, 2010; McDougall & Barker, 2011).

2.3.2. Calculation of Water Masses Fractions

To quantify fractions of water masses within the RT anticyclone, we adapted the mixing triangle method (Mamayev, 1975) and applied it to the wintertime ship-board data, collected at the RT southern entrance, ~53–54/55°N transect line (Figure 1a), where the properties of the water masses are less modified. Other methods exist, such as the Optimum Multiparameter (OMP)/extended OMP (Karstensen & Tomczak, 1998). For optimum weighting, they implement nutrients and oxygen data, which were not collected in January 2007 and January 2011. Triangle-based calculations without using nutrient and oxygen have proven successful in the past (e.g., Langehaug & Falck, 2012). Considering that water masses undergo changes along their pathways through various processes, we allow for water masses to vary within given parameter ranges, including a density range, instead of defining a single characteristic point as a condition for any parameter.

As any other user-defined water masses analysis, the mixing triangle method adopted here is sensitive to the choice of boundary conditions, imposed on water masses properties. Recognizing that our focus is on investigating the plausibility of MOW-rich anticyclones translating into the RT, and sustaining the RT anticyclone, and to avoid the introduction of preferential analysis, we allow for a wider SAIW density range, 27.25–27.65 kg m^{-3}, whereas MOW density condition is bound to its much narrower density range, 27.41–27.60 kg m^{-3}. Hence, we permit for a fair competition between the SAIW and MOW intermediate water masses, which reach the RT mainly through the NAC and slope current, respectively. For method's details, please see Appendix A.

2.3.3. Surface Imprint of the Deep Anticyclone

To identify the surface imprint of the anticyclone and the surrounding eddy field, we compute the Okubo-Weiss (OW) parameter (after Okubo, 1970, and Weiss, 1991) and the relative vorticity (ζ) using the weekly composite ADT. The OW parameter is widely used as an eddy detection method and is applicable to defining vortices in both altimetry and model output data sets (e.g., Chelton et al., 2011; Gula et al., 2016a; Isern-Fontanet et al., 2006). The OW parameter is taken as a quantification of strain versus vorticity and equal to $s_n^2 + s_s^2 - \zeta^2$, where s_n is the normal strain component, s_s the shear strain component, and ζ is the relative vorticity of the two-dimensional field (u and v the zonal and meridional components), with $s_n = \partial u/\partial x - \partial v/\partial y$, $s_s = \partial v/\partial x + \partial u/\partial y$ and $\zeta = \partial v/\partial x - \partial u/\partial y$ (Gula et al., 2016a; Isern-Fontanet et al., 2006; Petersen et al., 2013; Vortmeyer-Kley et al., 2016). Within eddy cores, vorticity amplitude manifests itself as a local maximum, thus outweighing the strain component, underlining eddy cores by characteristic negative OW parameter (Vortmeyer-Kley et al., 2016). Following Halo, Backeberg, et al. (2014) and Halo, Penven, et al. (2014), we impose OW < 0 criterion, thus allowing to define vortices of various sizes. No specific ADT threshold value is applied for determining eddies' boundaries, as we aim to capture not only circular but also multipoles/elongated ADT closed loops.

To quantify the anticyclone's imprint at the surface, we use the formula from Bashmachnikov and Carton (2012), which represents the effect of a deep eddy on the sea surface elevation as $SSE = (f^2 \times R^2 \times \Delta H)/(4 \times g \times H)$, with f, the Coriolis parameter, R the eddy radius, ΔH the isopycnal displacement, g the gravity acceleration, and H the depth of the eddy.

2.3.4. Ertel Potential Vorticity, Geostrophic Velocity, and Mixed Layer Depth From Hydrographic Data

When neglecting vertical velocity, the standard Ertel PV is

$$Q = \left[\frac{1}{g} \times (f + \zeta)N^2 + \frac{1}{\sigma_0} \times \left(\frac{\partial v}{\partial z}\frac{\partial \sigma_\theta}{\partial x} - \frac{\partial u}{\partial z}\frac{\partial \sigma_\theta}{\partial y} \right) \right] \tag{1}$$

with f the Coriolis parameter, ζ the relative vorticity, $N^2 = [-(g/\sigma_0) \times (\partial \sigma_\theta/\partial z)]$ the Brunt-Väisälä buoyancy frequency squared, g the gravity acceleration, u and v the zonal and meridional velocity components, and σ_θ the potential density referenced at the surface.

To calculate Ertel PV from observations (Q_{obs}), we follow Zhao, Bower, Yang, Lin, and Zhou (2018) approach. Assuming dominant northward/southward currents and predominant zonal density gradient along the transect line: (1) ζ can be approximated by $\partial v/\partial x$; (2) $\partial u/\partial z \times \partial \sigma_\theta/\partial y \ll \partial v/\partial z \times \partial \sigma_\theta/\partial x$. Thus, an approximate Ertel PV can be expressed as

$$Q_{obs} = \left[\frac{1}{g} \times \left(f + \frac{\partial v}{\partial x} \right) N^2 + \frac{1}{\sigma_0} \times \left(\frac{\partial v}{\partial z} \frac{\partial \sigma_\theta}{\partial x} \right) \right] \qquad (2)$$

The first term in Equation 2 represents the stretching vorticity, the last term denotes the horizontal vorticity component and buoyancy gradient product. As shown in Zhao, Bower, Yang, Lin, and Zhou (2018), the dominant term is the stretching term, which can be approximated by $Q_{str} = fN^2/g$. We use this simplified PV (Q_{str}) term to characterize PV anomalies from in situ data. To suppress and filter out small-scale and high-frequency motions, such as internal waves, a running mean with a window of 50 dbar is applied, following de Jong et al. (2012).

Following Marnela et al. (2016), GV (m s^{-1}) between stations pairs is computed from the CTD dynamic height data. The derived velocity profiles are calculated relative to a constant value/plane, where velocity is taken to be zero, considered a level of no motion (LNM). The LNM can be defined as the bottom topography boundary, the deepest common level between stations or boundary planes between water masses, or could be determined from ADCP data. Along-transect ADCP data are unavailable, and water masses boundaries in the region are nonuniformly distributed along the transect and in the vertical. Between adjacent stations there may be several layers with constant relative pressure differences; also, there could be no layer with constant pressure difference (Fomin, 1964). We thus considered LNM as the deepest common pressure between two consecutive stations. Where stations have not been sampled in a given year, consecutive CTD casts were used for calculations. Hence, we defined LNM to be the maximum pressure point of the shallower CTD cast/station in any given pair of casts/stations. Without knowledge of the velocity at LNM, this method only provides the GV relative to the LNM (Equation 3). We used the CTD-derived relative GV to provide an in situ estimation of the rotational direction of the anticyclonic vortex in complement of altimetry-based presentations.

$$GV \times f = -\frac{1}{\sigma_0} \frac{\partial \sigma_\theta}{\partial x} \qquad (3)$$

We calculated mixed layer depth (MLD) following de Boyer Montégut et al. (2004), as the depth at which σ_θ changes by 0.03 kg m^{-3} relative to σ_θ at 10 m depth.

2.3.5. Lagrangian Particle Tracking

We perform Lagrangian particles tracking experiments to investigate the origin of water masses in the RT anticyclone and test our hypothesis that the RT anticyclone is partly sustained by eddies shed from the slope current. Following Gula et al. (2014), neutrally buoyant particles are seeded into the model solutions in December 2011. Particles are advected by the model velocity fields backward in time for 2 years, without additional dispersion from the model's mixing processes. In total, 47,350 particles are released within the RT anticyclone, between 200 and 2,000 m depth, with a 50 m level-step. Initial horizontal distribution of particles at each depth level covers 3,844 km^2. Particles are advected using a Runge-Kutta 4 time-stepping scheme with a time-step of 120 s. Model outputs are stored with a 12 h period and are linearly interpolated in time to get sufficiently frequent sampling for accurate parcel advection. Velocity and tracer fields are interpolated at the positions of the particles using cubic spline interpolation in both the horizontal and vertical directions.

3. RT Anticyclone Structure From Ship-Board and Model Data

3.1. Signature From Ship-Board Data

The mean 2006–2013 CTD-derived AS, CT, and σ_θ vertical sections are shown in Figures 2a and 2d. The signature of the RT anticyclone is visible by the downward displacement of the 27.4–27.7 g kg^{-1} isopycnals at ~55.1°N, 12.6°W. Two prominent occurrences of the RT anticyclone occurred, in January 2007 and January 2011 (note no survey in 2008 and partial surveys in 2012 and 2013). The January 2007 and 2011 AS, CT, and σ_θ fields (Figures 2b, 2c, 2e, and 2f) show distortion of thermostads, halostads, and isopycnals at ~55.1°N, 12.6°W, capturing the extent of the RT vortex throughout the water column.

The anticyclone has a radius of ~39.5 km, corresponding to an averaged distance between CTD stations, which differs in different years and reaches down to ~1,550 m in both years, as shown by the vertical profiles of AS, CT, σ_θ, PV anomalies (Figure 3), and GV (Figures 4c and 4d). The RT subsurface anticyclonic vortex
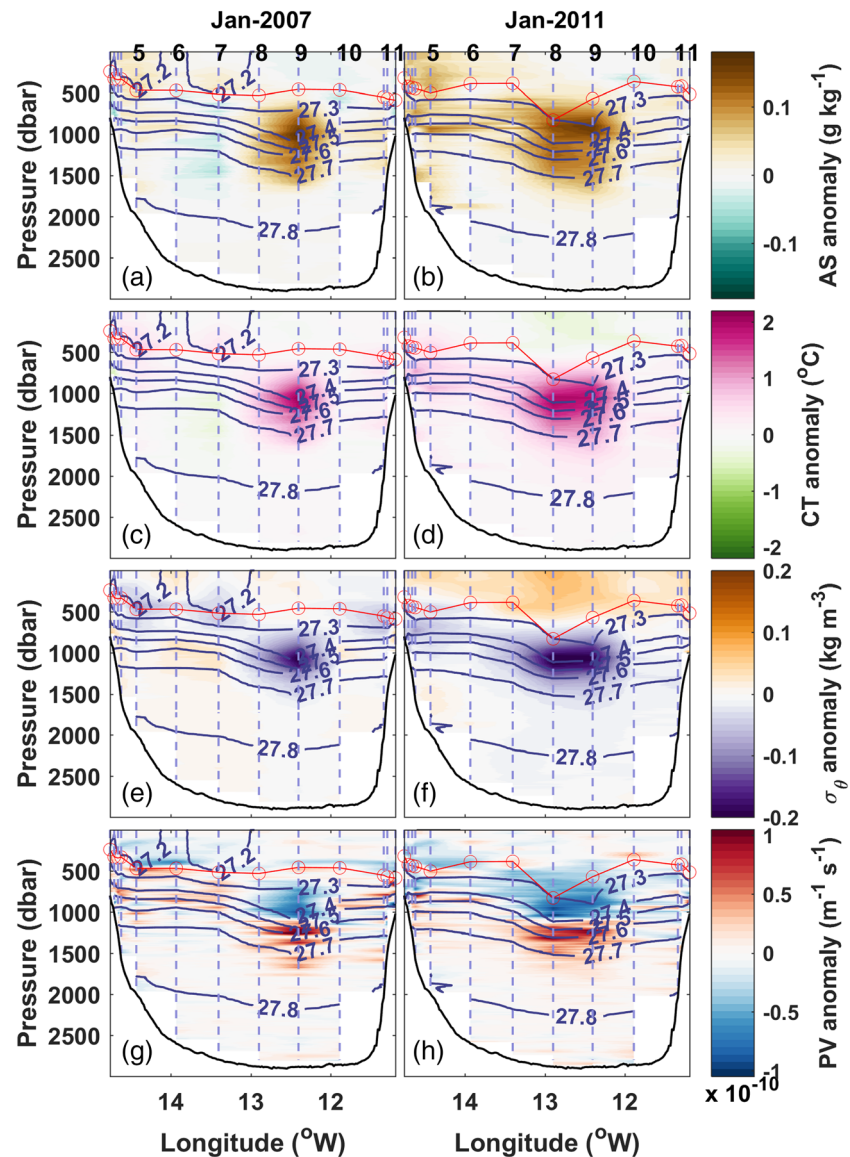
Figure 3. Longitude-pressure in situ-derived anomalies of absolute salinity (AS) (g kg^{-1}) in (a) January 2007 and (b) January 2011, conservative temperature CT (°C) in (c) January 2007 and (d) January 2011, potential density (σ_θ) (kg m^{-3}) in (e) January 2007 and (f) January 2011, stretching potential vorticity, PV (Q_{str}) = fN^2/g, (m^{-1} s^{-1}) in (g) January 2007 and (h) January 2011. Light gray dashed lines in all plots are representative of stations locations. Dark gray lines show σ_θ, referenced to 0 dbar. MLD is shown as a continuous red line. Anomalies are computed relative to the undisturbed background (Figure S4).

region is defined as per criteria outlined in section 2.3.1. In both years, the thickness of the vortex core is very similar. It stretches over 900–950 m in the vertical, within ~600–1,550 m in 2007 and ~650–1,550 m in 2011. The depths of the upper and lower boundaries of the core region are subjectively approximated to the respective depths at which the first instance of doming and the last instance of downward curving of isopycnals are observed. In both 2007 and 2011, the vortex core is centered within the 27.3 and 27.6 kg m^{-3} isopycnals. The GV associated with the anticyclone extends from the surface to 1,550 m depth with a maximum of 0.3 m s^{-1} around 500 m depth (Figures 4c and 4d). In both years, a negative PV anomaly is visible in the anticyclone's core, accompanied by high PV anomalies, between 0.7×10^{-10} and 1.1×10^{-10} m^{-1} s^{-1}, located just below the core (Figures 3g and 3h). Mean AS, CT, and PV anomalies in 2007 and 2011 along the vortex core and highest AS, CT, and PV anomalies, found within the anticyclone's core, are presented in Table S3.
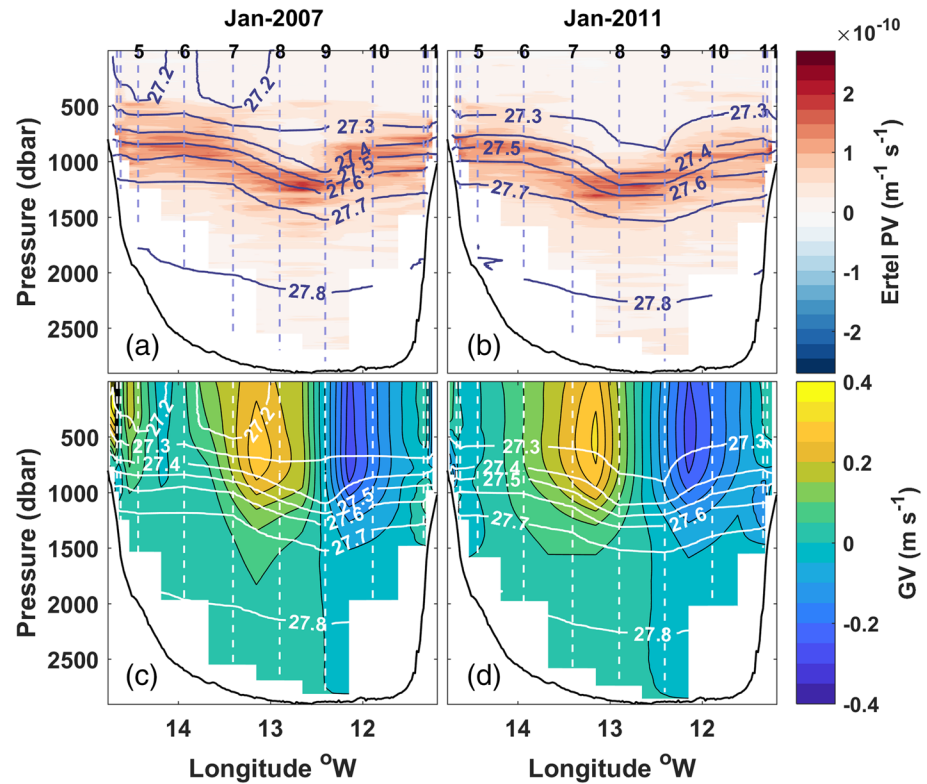
Figure 4. PV (Q_{obs}) (m^{-1} s^{-1}) in (a) January 2007 and (b) January 2011 and in situ-derived geostrophic velocities (GV) (m s^{-1}) in (c) January 2007 and (d) January 2011. Light gray/white dashed lines represent stations locations, that is, vertical profiles, with deep stations numbered on top of panels. Solid dark gray/white lines depict potential density (σ_θ) (kg m^{-3}), referenced to 0 dbar.

The anticyclone is well captured by the PV (Q_{obs}, Equation 2) distributions in both January 2007 and January 2011 (Figures 4a and 4b). PV values are close to zero in the core's upper region. In both January 2007 and January 2011, there is a consistent, seemingly uninterrupted band of positive PV, confined within the 27.4–27.7 kg m^{-3} isopycnal surfaces, regionally corresponding to the heavier/inner MOW density range.

This band of positive PV captures the permanent pycnocline, where the local maximum stratification is found. It stretches between ~800 m down to ~1,000 m, with a very pronounced deepening down to ~1,200 m, resulting from the presence of the RT vortex core. The slanting of the isopycnals, typical of anticyclones, is due to the intensified anticyclonic rotation at depth, as evident from the across-transect GV snapshots (Figures 4c and 4d). The pycnocline depth corresponds well with Argo-based computation from Feucher et al. (2016), who estimate it between ~800 and ~1,000 m depth (Figure 7a in their study).

3.2. RT Anticyclone Water Masses

Four distinct water masses (ENACW, SAIW, MOW, and LSW) are visible in the southern RT in both the ship-board CTD data (Figures 5a and 5b) and the WOA18 data set (Figures 1b–1d). However, the water masses characteristics are less distinct within the central RT (Figure 5c) and further smoothed and eroded within the RT anticyclone (Figure 5d).

Water masses mixing is apparent when comparing the T/S diagrams from the southern (~53–54/55°N) and central (~54–56°N) RT transect lines (Figures 5b and 5c). Within the RT, SAIW and lighter MOW share the same density, as do heavier MOW and LSW. It is thus possible that isopycnal mixing between SAIW, MOW, and LSW actively contributes to water masses modifications.

The mixing of water masses within the RT anticyclone is also likely stimulated by wintertime convection events, which can trigger vertical mixing between MOW, SAIW, and ENACW. A strong convective event is notable in January 2011, where MLD in the core of the RT anticyclone reaches ~830 m, whereas in January 2007, the MLD is ~460 m (Figure 3).
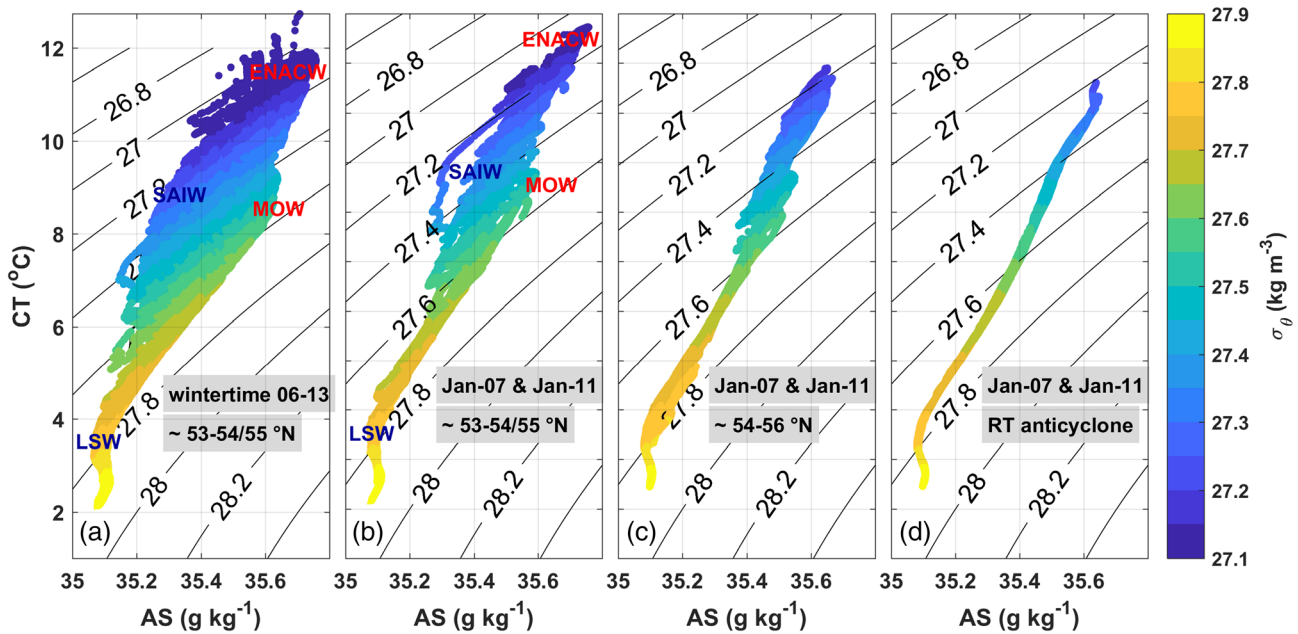
Figure 5. CTD-derived T/S diagrams for (a) all 2006–2013 wintertime CTD data, collected along ~53–54/55°N (Figure 1a) and used in the mixing triangle method (subsection 2.3.2), (b) January 2007 and January 2011 CTD data from ~53–54/55°N transect line, (c) January 2007 and January 2011 along ~54–56°N and (d) within the RT anticyclone at stations 8 and 9, cutting through the RT anticyclone's core in January 2011 and January 2007.
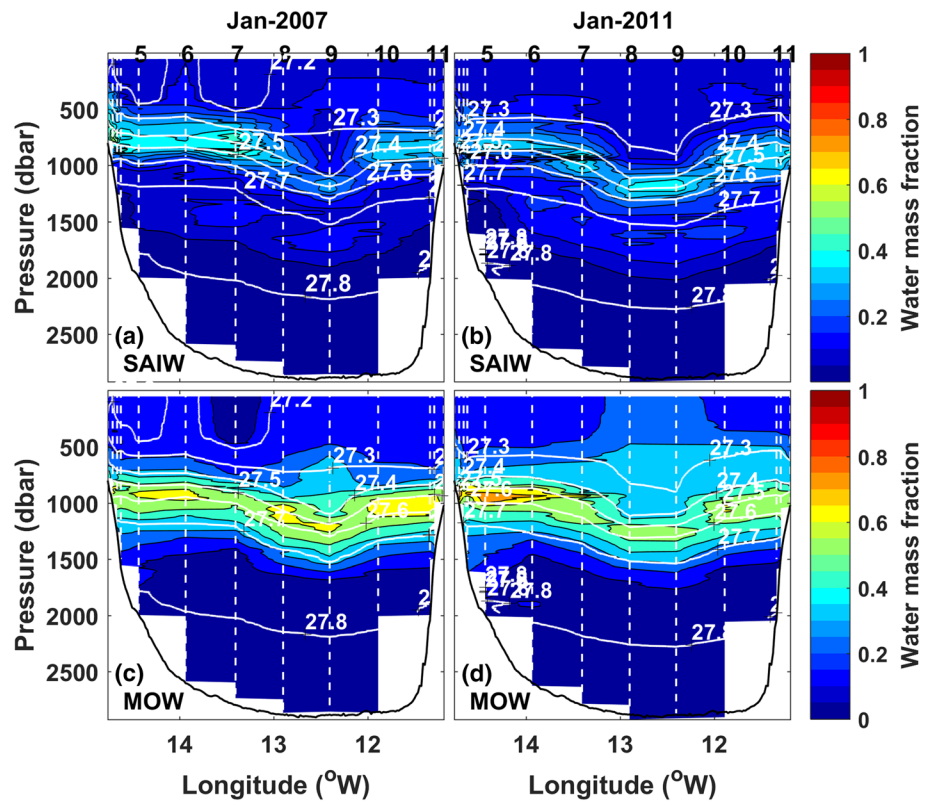

Figure 6. (a, b) SAIW fractions in January 2007 and January 2011 and (c, d) MOW fractions in January 2007 and January 2011, respectively. White dashed lines represent stations locations, that is, vertical profiles, with deep stations numbered on top of panels. Solid white lines depict potential density (σ_θ) (kg m^{-3}), referenced to 0 dbar.

The CTD-based water masses analysis shows that in January 2007, the SAIW fraction within the anticyclone's core is less than 25% (Figure 6a), whereas the MOW quantity is about 50–65% (Figure 6c). A similar trend follows in January 2011, where SAIW represents about 35% (Figure 6b) and MOW about 55% of the anticyclone's core content (Figure 6d). In both January 2007 and January 2011, MOW occupies the space within ~27.3–27.7 kg m^{-3} isopycnals, also evident in the PV (Figures 4a and 4b) vertical distribution. The occurrence of a stronger convective episode in January 2011 could explain the slightly smaller, or more mixed, MOW portion compared to 2007 (Figure 6d).

MOW is the main contributor to the RT anticyclone's core and potentially the main source of heat and salt within the RT. Despite the restrictive density boundary condition imposed on MOW, and the broad density range bound on SAIW, the water masses analysis yields high MOW proportions both within the RT anticyclone and laterally within the central RT. It is thus possible that MOW is present in even higher quantities and SAIW in lower quantities than what is estimated here.

3.3. Available Heat and Salt Content Anomalies

As subsurface vortices can transport water masses with anomalous properties over long distances, they have the potential to cumulatively affect large-scale transports of heat, salt, and other tracers (Gula et al., 2019). Stirring and filamentation processes at the periphery of coherent eddies are suggested to drive meridional eddy transports (Abernathey & Haller, 2018); hence vortices could alter ambient waters as they translate across various oceanic regions and basins. Below, we compute available heat and salt content anomalies to highlight the potential impact of the RT anticyclone on the regional and larger scale northeast NA heat and salt regimes, and its potential capacity to contribute to water masses modifications locally and further afield.

As all other anomalies, available heat and salt anomalies, AHA (J m^{-1}) and ASA (kg m^{-1}), respectively, were calculated relative to mean values for 2006, 2009, 2010, and 2013 (Figure S4), hence, the undisturbed background. Following Chaigneau et al. (2011), AHA and ASA per meter in the vertical can be derived by solving

$$AHA = \int \sigma_\theta C_p CT_a dA \qquad (4)$$

and

$$ASA = 0.001 \int \sigma_\theta AS_a dA \qquad (5)$$

In Equations 4 and 5, dA is the area (m^2) of the anticyclone, assumed to be delimited by a circle, and σ_θ as previously defined. C_p in Equation 4 is the specific heat capacity (~4,000 J kg^{-1} K^{-1}) and CT_a stands for conservative temperature anomaly. AS_a in Equation 5 stands for absolute salinity anomaly, where the factor 0.001 represents the conversion of salinity to salinity fraction (kg of salt per kg of seawater) (Chaigneau et al., 2011). AHA and ASA calculations were performed over the entire water column, assuming hypothetical anticyclone stretching from the surface to the bottom. This assumption will help with the deduction of the anticyclone's nature, whether (a) the anticyclone is a result of an upper ocean current, that is, NAC instability, or (b) the anticyclone is a deep vortex with waters originating from the MOW-rich deep core(s) slope current. If the waters within the anticyclone are originating from upper ocean water masses, that is, NAC (sub)branch waters, AHA and ASA in the upper (0–500 m) water column are expected to be high. AHA and ASA show clear intermediate water column positive anomalies, confined within the defined anticyclone depth ranges (600–1,550 m in 2007 and 650–1,550 m in 2011) with peaks between 990–1,100 m depth (Figure 7). This indicates that the MOW can be a significant contributor to the deep AHA and ASA, a possible explanation would be the trapping of MOW during eddy generation. The calculated AHA and ASA for January 2006, February 2009, and February 2010, when the anticyclone is not falling along the survey transect line, all yield no significant anomalies within the designated anticyclone's depth range. AHA and ASA for February 2009 and January 2013 show small positive contributions from about ~700 m down to ~1,600 m and from ~500 m down to ~1,200 m, respectively. In February 2009, the surface imprint of the anticyclone is positioned just south of the transect midpoint (Figure 8d), whereas in January 2013 (Figure 8h), the surface imprint of the anticyclone is located just north/northeast of the transect midpoint. Thus, it is possible that the anticyclone's rim was sampled by the CTD at depth (note that an exact collocation between the surface imprint and the anticyclone's core at depth is not expected; furthermore, CTD rosette would be carried
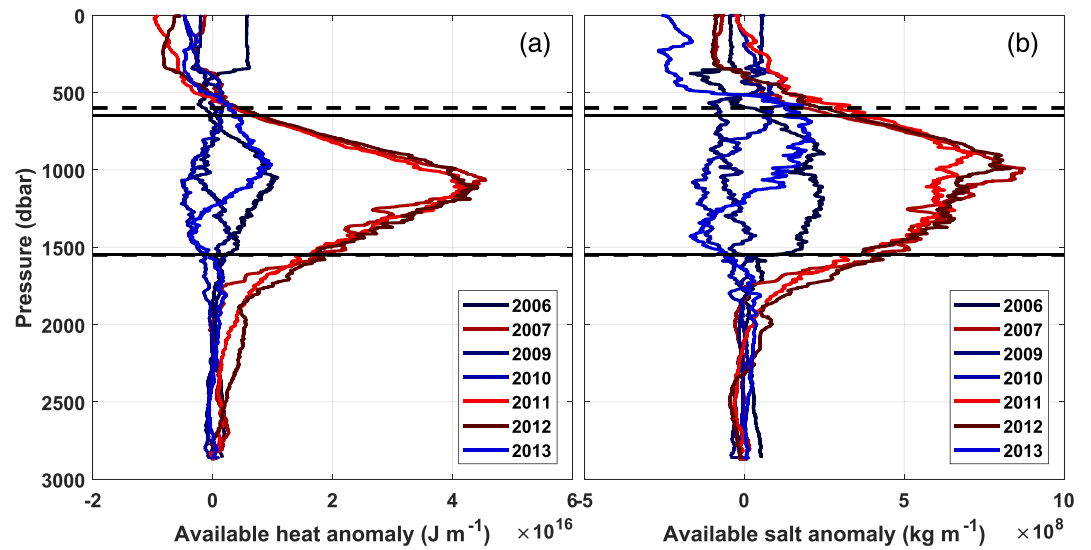
Figure 7. (a) Available heat anomaly (AHA) (J m^{-1}) and (b) available salt anomaly (ASA) (kg m^{-1}) with respect to depth over anticyclone defined circle area A (A = πr^2, r, anticyclone radius). Thick dashed black lines in both figures denote the anticyclone's core top (~600 m) and bottom (~1,550 m) boundaries in January 2007, whereas thick black lines representative of the anticyclone's core top (~650 m) and bottom (~1,550 m) boundaries in January 2011. AHA and ASA calculated relative to mean values for 2006, 2009, 2010, and 2013, representing the undisturbed background.

some distance away from the sampling stations, depending on magnitude and direction of the subsurface flow). AHA and ASA for January 2012 are close to calculated AHA and ASA anomalies for January 2007 and January 2011. Mean January 2007, January 2011 AHA and ASA values, calculated along the central vortex axis, and maximum core values are summarized in Table 1.

3.4. Surface Imprint of the RT Anticyclone

The weekly composite ADT maps (Figure 8), overlapping with surveys during the 2006–2013 wintertime period, encapsulate the mesoscale field within the RT region. The surface signatures of anticyclonic vortices are visible in all weekly ADT composites. The RT anticyclone is identified as the largest anticyclonic (blue colored) vortex in the central RT. Further, the RT anticyclone position coincides with the lowest negative OW parameter estimates for each corresponding ADT composite period.

The RT anticyclone maintains a nonstationary position. It shifts between ~54–54.5°N to 56°N, and 11.8°W to 13.5°W longitude, that is, within 1–1.5° latitude/longitude of its preferential location at 55°N, 12°W. In 2007, 2011 and 2012, the anticyclone's surface signature crosses the transect line (Figures 8b, 8f, and 8g). But in 2006, 2009, 2010, and 2013, the surface imprint is positioned either northeast or southwest of the transect line (Figures 8a, 8d, 8e, and 8h), thus explaining the absence of the vortex signature in the CTD transects (note no survey in 2008).

To examine the RT anticyclone's influence on the surface elevation, we apply a formula, derived by Bashmachnikov and Carton (2012), for the estimation of meddy's imprint on the sea surface elevation (section 2.3.2). The application of the formula for the RT anticyclone yields a surface elevation of 0.26 m, due to the presence of the anticyclone at depth. This is in good agreement with the ADT-derived surface elevation value of 0.25 m in both January 2007 and January 2011 (Figures 8b and 8f). The surface elevation estimate of 0.26 m is based on aggregate January 2007 and January 2011 values, where $f = 1.19 \times 10^{-4}$ s^{-1}, RT anticyclone radius = 39 km, $\Delta H = 500$ m, $g = 9.81$ m s^{-2}, and $H = 1,063$ m. The RT anticyclone radius, ΔH and H approximated values are based on ship-board data, as defined in section 2.3.1.

3.5. The RT Anticyclone in the Model

The model simulation captures well the presence and the nonstationary nature of the RT anticyclone. In the model, the RT anticyclone is at times centered between ~54.5–55.5°N and ~12–13°W latitude and longitude bands. The vortex exhibits low relative vorticity values, reaching down to −0.3f and beyond (Movie S1).
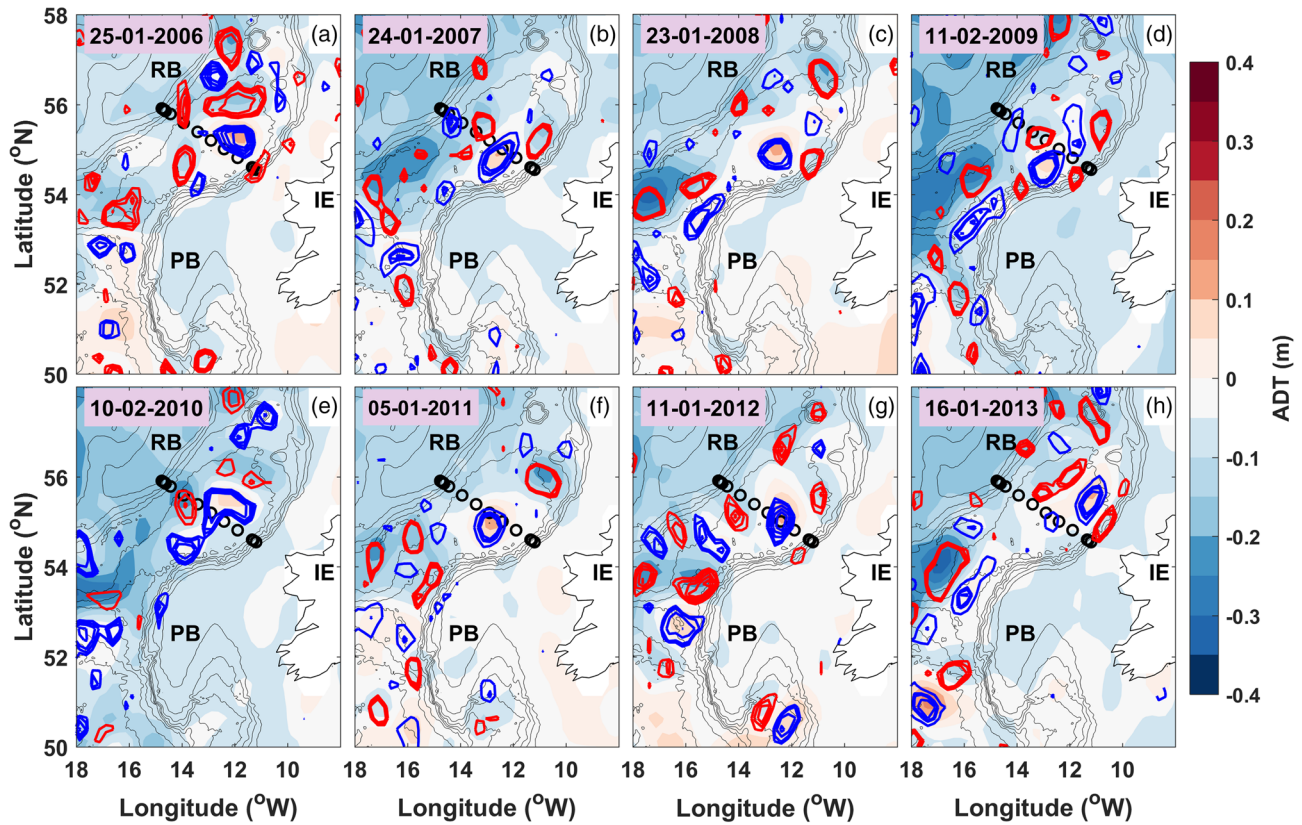
Figure 8. Seven-day mean ADT maps from satellite altimetry with contours of relative vorticity, ζ. Contours of cyclonic (blue) and anticyclonic (red) vortices vary within 0.1 to 1.6×10^{-4} s^{-1} and -1.6 to -0.1×10^{-4} s^{-1} positive and negative relative vorticity ranges, with all vortices satisfying Okubo-Weiss (OW) parameter <0. Dates in each weekly ADT composites (a–h) represent the start of the week, coinciding with respective wintertime ship-board survey periods. Light-gray lines show bathymetry (500 m level-step), black circles denoting survey transect line stations (note no survey in 2008). Letter annotations as in Figure 1.

The model also represents well the regional thermohaline properties and the vertical structure of the RT anticyclone. Examples of model-derived wintertime AS and CT anomalies (relative to 2001–2009 mean) distributions in the vertical are presented for January 2007 (Figures 9a and 9b), where model and observations locate the RT anticyclone with great proximity. In the model, the January 2007 AS anomaly (Figure 9a) is larger than the in situ-derived AS anomaly (Figure 3a), with a positive difference of approximately 0.03 g kg^{-1} within the anticyclone's core. The model captures well the CT anomaly (Figure 9b) comparative to observations (Figure 3c), particularly within the anticyclone's core region with core CT anomalies of approximately 1.15°C in both data sets. The σ_θ field, notably intermediate and deep water column depths, is also well represented in the model (Figure 9) comparative to observations (Figures 3a, 3c, 3e, and 3g).

The regional PV (Equation 1) and GV are also well reproduced by the model. The continuous band of positive PV, confined within the 27.3–27.7 kg m^{-3} isopycnals is present both in the model and the CTD data. The

Table 1
In Situ Derived Available Heat and Salt Anomalies (AHA, ASA) Values in January 2007 and January 2011

	2007		2011	
Anomaly	Overall anticyclone's anomaly	Anomaly within the core center	Overall anticyclone's anomaly	Anomaly within the core center
AHA (J m^{-1} [×10^{16}])	2.67 (±1.12)	4.55 (1,066 m)	2.76 (±0.89)	4.26 (1,129 m)
ASA (kg m^{-1} [×10^8])	5.95 (±1.58)	8.76 (993 m)	5.66 (±0.96)	7.59 (905 m)

Note. ±1 standard deviation values are enclosed in brackets; maximum AHA and ASA values are also presented, found within anticyclone's core regions, embedded within the 600–1,550 m and 650–1,550 m depth ranges in 2007 and 2011, respectively. AHA and ASA are calculated relative to undisturbed background, thus mean values for 2006, 2009, 2010, and 2013.
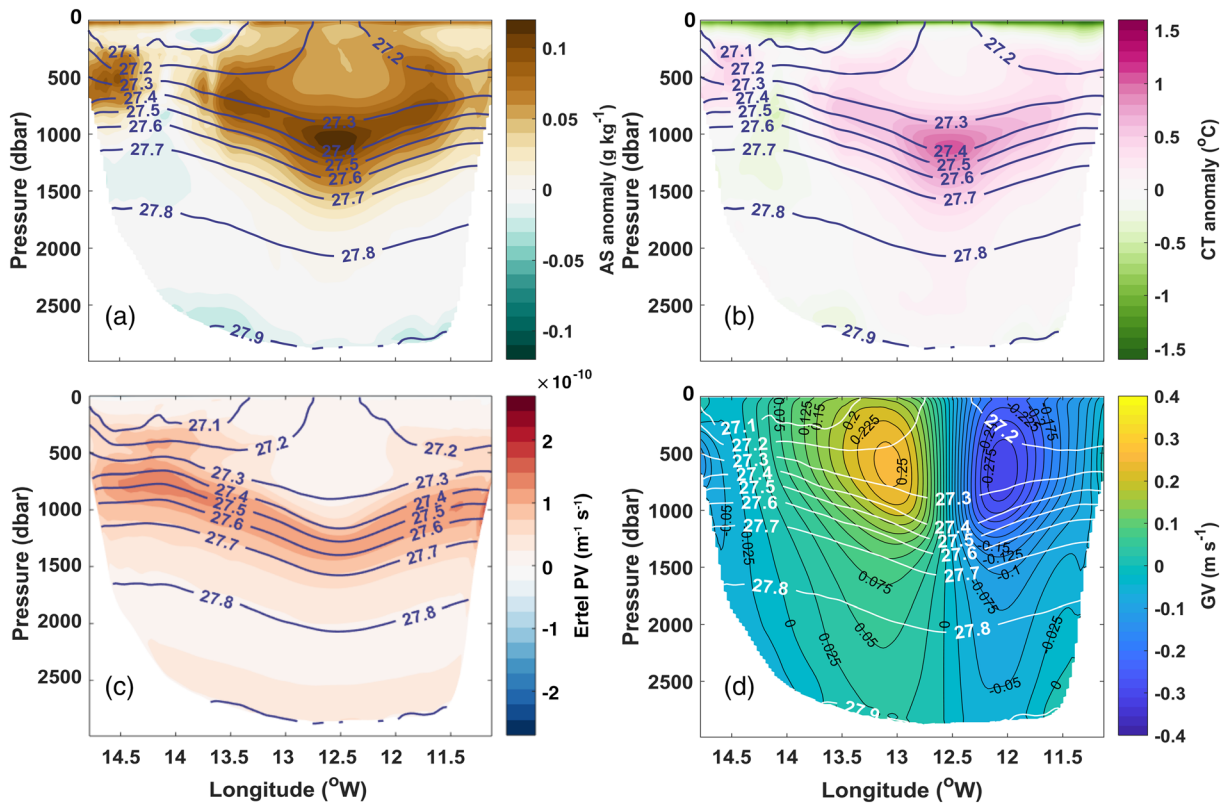
Figure 9. Longitude-pressure model-derived a) absolute salinity (AS) anomaly (g kg^{-1}), b) conservative temperature (CT) anomaly (°C), c) PV (Equation 1) (m^{-1} s^{-1}), and d) geostrophic velocity (GV) (m s^{-1}), depicted by solid black contour lines. Solid dark/white grey lines in all plots show the potential density (σ_θ) (kg m^{-3}), referenced to 0 dbar.

model-derived GV reaches a maximum of 0.225 m s^{-1} around and below 500 m depth. This is slightly lower than the CTD-derived maximum GV of 0.3 m s^{-1} for January 2011 (Figures 4c and 4d). Overall, the model gives sufficiently realistic replicates of the anticyclone and ambient surroundings.

4. RT Anticyclone Driving Mechanisms

Given the realistic representation of the RT anticyclone structure in the model, we can use model data to study the driving mechanisms of the anticyclone. In this section we investigate the dynamical processes that generate and control the RT anticyclone by looking at the evolution of relative vorticity and PV in the framework of Lagrangian experiments. Then we use the same experiments to describe the origin of the water masses that compose the core of the anticyclone.

4.1. Generation of the RT Anticyclone Through Nonlinear Turbulent Processes

The RT anticyclone is always present during the studied period both in satellite observations (Figure 8) and in the model (Movie S1). To investigate the formation of the anticyclone, we thus reinitialize the North-Atlantic parent simulation on 1 January 2009 based on the corresponding monthly SODA reanalysis, where no anticyclone is present. The model setup is identical to the one of the original simulation (see section 2.2.1). The evolution of relative vorticity in the RT is shown at different instants during 2009 in Figure 10. We show the relative vorticity interpolated on the 27.3 kg m^{-3} isopycnal surface, which forms the upper boundary of the anticyclone's inner core in observations (Figure 3) and in the model (Figure 9).

Neither cyclones nor anticyclones are initially present in the RT. Small scale positive and negative vorticity structures appear progressively during the first few weeks of the simulation. They are initially generated along the RT boundaries (Figure 10a), progressively advected toward its center (Figure 10b), filling the entire RT after a few months (Figure 10c). Several merging events between anticyclones are visible during the
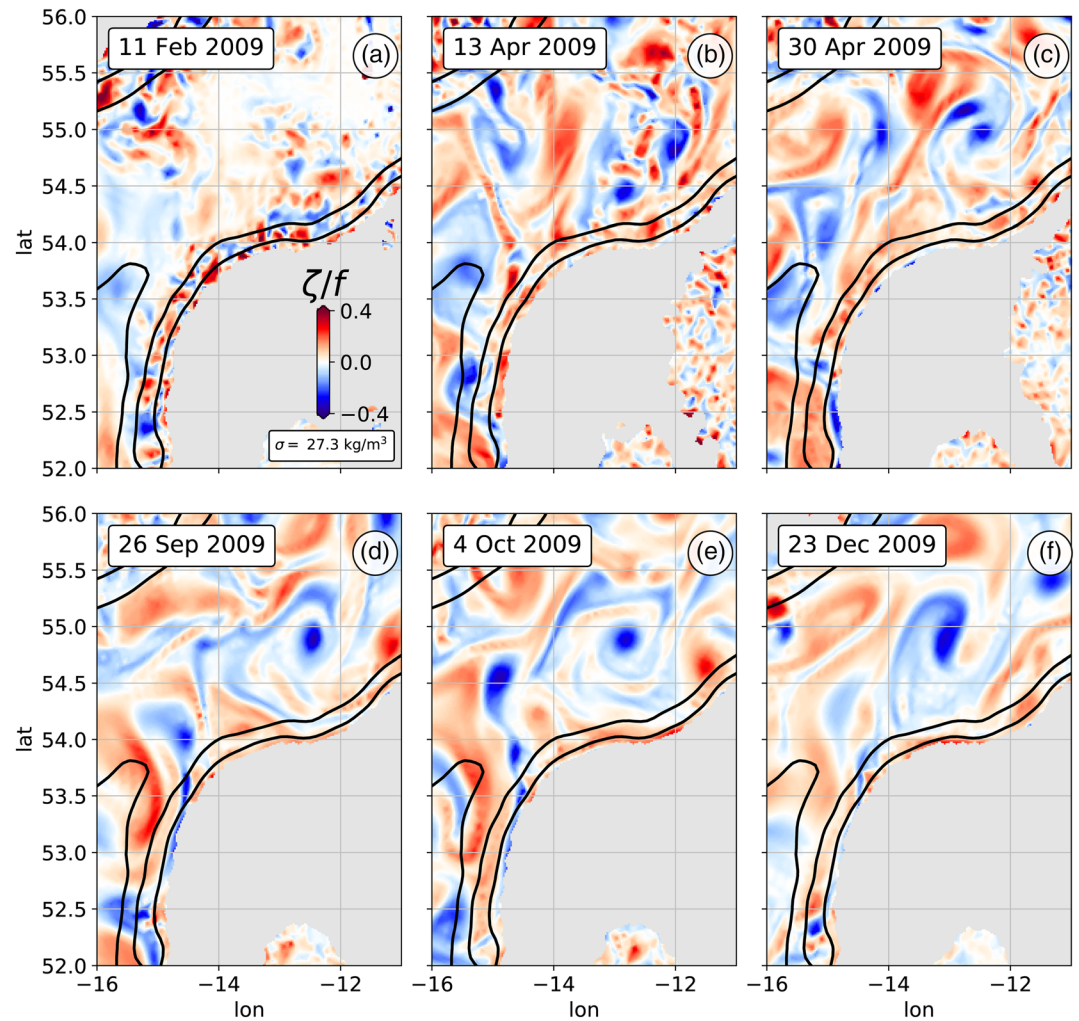
Figure 10. Model-derived relative vorticity normalized by f, ζ/f, on the 27.3 kg m^{-3} isopycnal during the spin-up of the parent simulation (dx $\approx$ 6 km). No anticyclone is initially present in the RT, but the merging of smaller scale anticyclones leads to the formation of the RT anticyclone after a few months.

following months (Figure 10c) leading to the formation of larger anticyclones until reaching the size and amplitude of the RT anticyclone (Figures 10d–10f). The RT anticyclone then keeps being fed by smaller anticyclones throughout the whole simulation. The small scale anticyclones are generated along the boundary, in particular along the PB slope (Figures 10d and 10e).

The RT anticyclone is not here a direct result of a baroclinic or barotropic instability of a larger scale current. Instead it is the result of nonlinear turbulent processes that are driving energy from small to larger horizontal (and vertical) scales. Such an inverse cascade of energy is typical of the quasi-geostrophic turbulence regime that is expected to prevail in the ocean for geostrophic mesoscale structures (e.g., Assene et al., 2020; Schubert et al., 2020).

4.2. Dynamical Processes Sustaining the RT Anticyclone

The merging of smaller anticyclones with the RT anticyclone appears to be an important mechanism to sustain the RT anticyclone and feed it with negative vorticity and low PV. Another likely candidate is the wintertime convection, which can generate deep mixing and bring low PV in the core of the RT anticyclone. Both processes have been suggested as important to sustain similar examples of deep quasi-permanent anticyclones (Bosse et al., 2019).
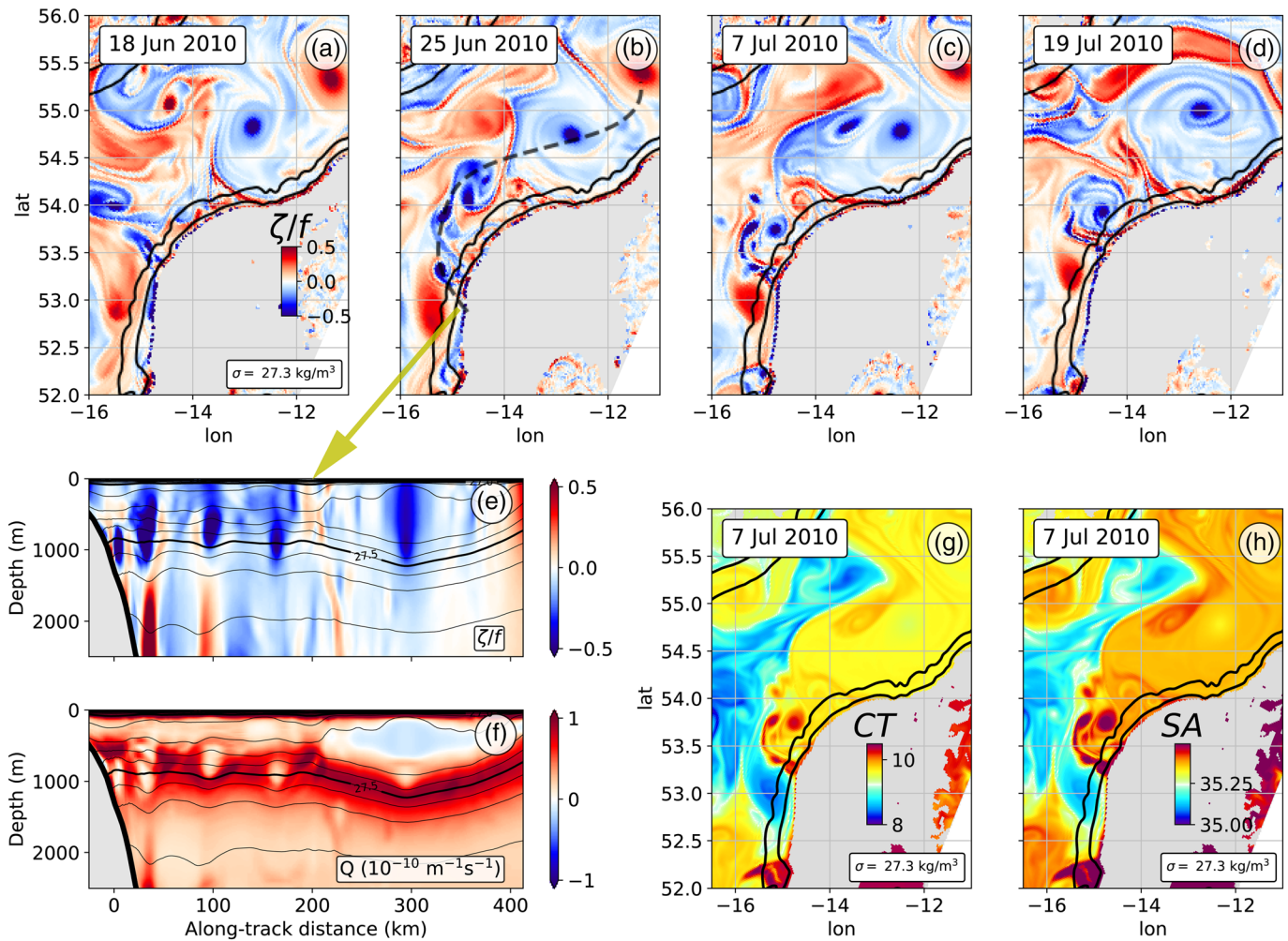
Figure 11. Model-derived relative vorticity, normalized by f, ζ/f, on the 27.3 kg m^{-3} isopycnal at four different times (a–d). (e) Vertical sections of relative vorticity and (f) PV at the time of panel (b). The position of the section is indicated as a dashed line in panel (b). (g) Conservative temperature and (h) absolute salinity on the 27.3 kg m^{-3} isopycnal at the time of panel (c).

4.2.1. Merger of Anticyclonic Vortices Shed From the Slope Current

Merging events are happening regularly throughout the whole 2002–2011 period in the higher resolution simulation (dx ≈ 2 km) typical example is shown in Figure 11. More examples are provided in Figures S5 and S6 and the full period is visible in Movie S1.

Vorticity snapshots depict the generation of anticyclonic vorticity along the Porcupine Bank (PB) slopes south of 53.5°N, the detachment of vorticity filaments around 53.5°N, and the formation of coherent anticyclonic structures due to the filaments rolling up (Figure 11). The anticyclones are generated predominantly in the density range 27.3–27.6 kg m^{-3}, which corresponds to the density range of the RT anticyclone's core. The anticyclones are then advected into the interior of the trough along isopycnals and eventually merge with the RT anticyclone (Figure 11c).

This sequence of vorticity generation, bottom boundary layer separation, and formation of coherent (sub) mesoscale cyclonic/anticyclonic vortices is similar to the sequence described in D'Asaro (1988), Molemaker et al. (2015), Gula et al. (2015, 2016b), and Vic et al. (2015). A boundary slope current moving anticyclonically/cyclonically around a basin (meaning that the flow has the coast on its left/right in the Northern Hemisphere) generates highly positive/negative relative vorticity and potential vorticity values within the sloped turbulent bottom boundary layer. The narrow negative vorticity stream is seen developing regularly within the 51–53.5°N latitude band, where the current flows northward along the PB (Figures 10 and 11, Movie S1). The importance of frictional effects for the generation of vorticity along the PB slopes is

shown in Le Corre et al. (2019) through an analysis of the PV fluxes at the bottom over the whole simulation period, with the strongest negative PV input found between the 27.3 and 27.6 kg m^{-3} isopycnals. The vorticity filament separation and anticyclones pinch off occur at two preferential spots due to the topographic curvature and flow inertia: near 52°N, where a sharp break in the shelf edge exists, and near 53.5°N, where the shelf edge and Porcupine Ridge turn eastward. Once detached from the boundary, the fine-scale ζ/f fragments begin to move chaotically by mutual advection, promoting merging during close encounters, ultimately leading to both horizontal and vertical growth size, resulting in the generation of a (sub)mesoscale size vortex (Molemaker et al., 2015; Srinivasan et al., 2019).

Most of the formed small-scale anticyclones are advected in the RT interior where they ultimately merge with the RT anticyclone. The process is typical of vortex mergers, in which two like-signed coherent vortices collapse when they get closer to a critical distance of about 2.5R, with R the vortex radius (Ciani et al., 2016; de Marez et al., 2020). Some of the smaller mesoscale/submesoscale anticyclones, generated along the PB slope, can also propagate westward, around the Rockall and Hatton banks and into the eastern subpolar NA (Figures 10, 11, S5, and S6, Movie S1), depending on the surrounding mesoscale activity.

Merging events can also be identified with the use of satellite altimetry data (e.g., Le Vu et al., 2018). A merging event is visible in February 2010 (Figure 8e) as a medium-sized anticyclonic vortex pinches off the northern tip of the PB, near 54.5°N 14.5°W, and joins the RT anticyclone. A more quantitative assessment of the frequency of merging events based on satellite data may be possible. However, given their small horizontal scales and intensification at depth, the anticyclones generated along the PB have a weak surface signature (Figures 11e and 11f). Thus, only the bigger ones, which have been growing in scales before merging with the main RT anticyclone, may be detectable in satellite altimetry.

4.2.2. Impact of Wintertime Convection and Eddy Merger on the RT Anticyclone

To quantify the importance of eddy mergers and wintertime convection in feeding low PV to the RT anticyclone, we perform a Lagrangian experiment and diagnose PV transformations along the Lagrangian trajectories. We seed neutrally buoyant Lagrangian particles inside the anticyclone at the end of the simulation (December 2011) and compute their backward trajectory during the two preceding years. The position of the particles at seeding time is defined based on the position of the center of RT anticyclone and a $\zeta/f < -0.1$ condition (Figures 12a and 12b), such that only particles initially inside the RT anticyclone are considered.

The position of particles over the 2010–2011 period is shown in Figure 12a. Most particles do not leave the RT over the period. Two main paths for particles getting inside the RT are visible: one in the south-east part of the RT, flowing northward along the PB, and one in the north-west part of the RT, flowing southward along the RB.

PV is conserved along Lagrangian trajectories, except in the presence of frictional or diabatic effects (Haynes & McIntyre, 1987; Marshall et al., 2001; Morel et al., 2019). Thus we can track the occurrences of such frictional or diabatic effects by computing PV changes along the Lagrangian trajectories ($\frac{dQ}{dt}$ in m^{-1} s^{-2}). The mean PV changes that particles of the RT anticyclone undergo at each location between January 2010 and December 2011 are shown in Figure 13b. The PB slope, between 51°N and 53.5°N, stands out as the region where the strongest PV changes occur, due to frictional and diabatic effects related to current-topography interactions.

To evaluate the integral impact on the PV budget of the RT anticyclone, the density of particles at each location needs to be taken into account. We have shown that large PV changes happen along the PB slope, but they involve only a fraction of the particles. So we need to integrate PV changes over the water volume represented by each particle to evaluate their overall importance. Time and volume-integrated PV changes ($\iiiint \frac{dQ}{dt} dV dt$ in m^2 s^{-1}) are shown in Figure 13c. The PB slope remains the region where the amplitude of the PV changes is the largest (-9.7 m^2 s^{-1}). However, another region stands out, which corresponds to the location of the RT anticyclone and where PV changes integrate the effects of both deep winter mixing and dynamical instabilities of the anticyclone (e.g., centrifugal, symmetrical, and mixed-layer baroclinic instabilities), amounting to -3.4 m^2 s^{-1}.
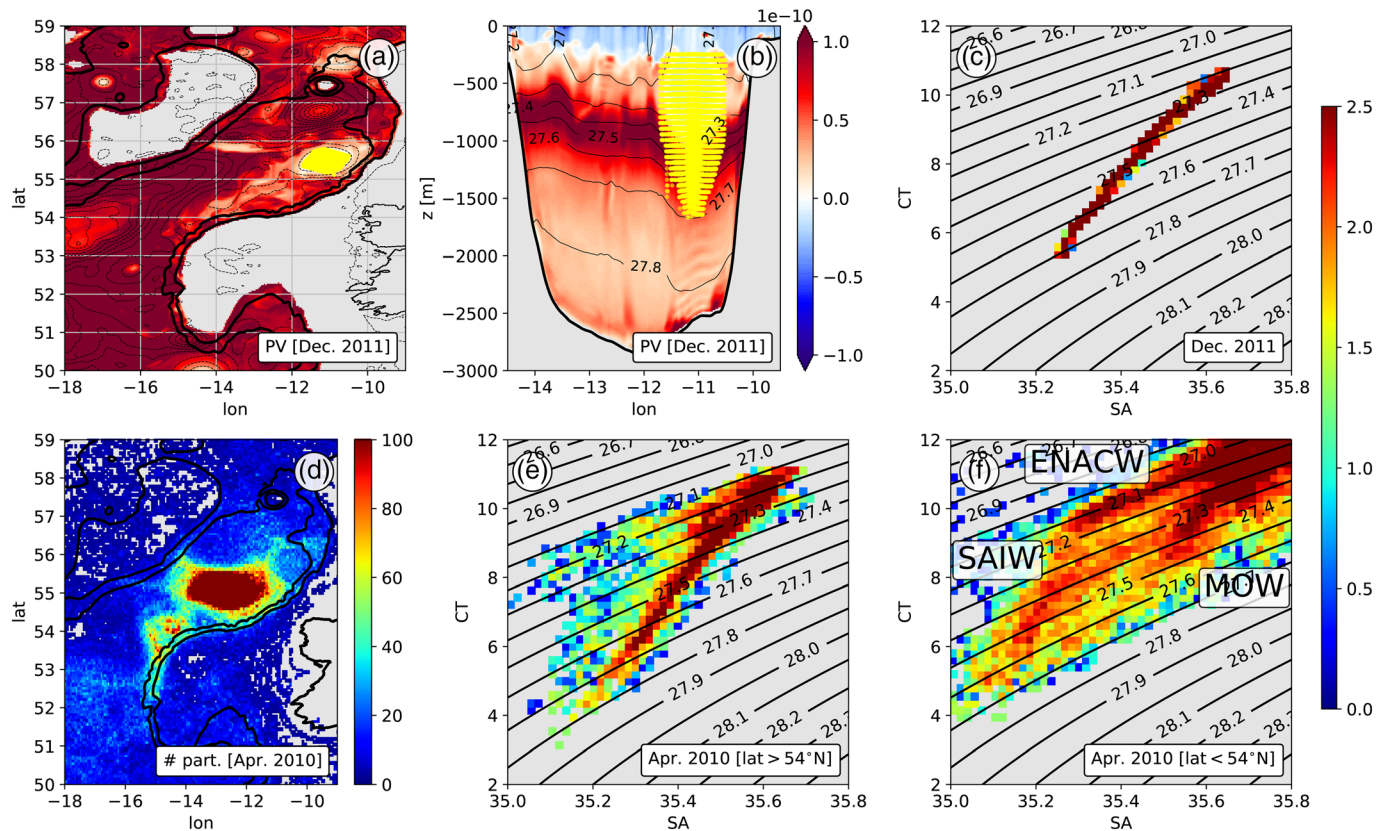
Figure 12. Particles position in (a) the horizontal and (b) vertical in December 2011 at the time of seeding. (c) Logarithmically scaled histogram of T/S characteristics of the particles at the time of seeding. (d) Particles position in April 2010 and (e, f) logarithmically scaled histogram of T/S characteristics in April 2010 for particles located (e) north and (f) south of 54°N.

Time-series of PV changes integrated over the two regions (shown as boxes in Figure 13c) are presented in Figures 13d and 13e for particles lighter or denser than 27.26 kg m^{-3}. The denser particles undergo PV changes along the PB slope, always leading to a PV reduction. However, they can undergo positive PV changes due to diabatic effects when merging with the RT anticyclone (Griffiths & Hopfinger, 1987). The lighter particles do not undergo PV changes along the PB slope but undergo strong events of negative PV changes at the location of the RT anticyclone. These events correspond to wintertime convection episodes from January 2010 to March 2010 and from December 2010 to March 2011. Due to the low stratification in the core of the anticyclone serving as a preconditioning, the convection can reach down to about 1,000 m, leading to strong diapycnal mixing, injection of potential energy and a re-energization of the RT anticyclone. A slight positive PV change is visible right after the convective event, which may be related to the spring restratification or to an centrifugal/symmetric instability of the RT anticyclone, leading to PV homogenization between the low PV inside the core and positive PV of the surrounding waters.

This PV budget highlights the importance of two processes in the generation and control of the RT anticyclone. One is the merging with smaller scale anticyclones generated along the PB slope, which continuously feed the anticyclone with low PV waters throughout the year. The other one is the wintertime mixing, which reduces PV in the core of the anticyclone and likely re-energize the anticyclone during winter.

4.3. Water Masses Origin and Mixing

What do these processes imply in terms of water masses and mixing for the RT anticyclone?

Anticyclones generated along the PB slope transport predominantly MOW. The northward flowing current along the PB slope is made of MOW in the range 27.3–27.7 kg m^{-3} (Figure 1), which coincides with the density range where anticyclones are generated due to flow-topography interactions (Figure 11). Figures 11g
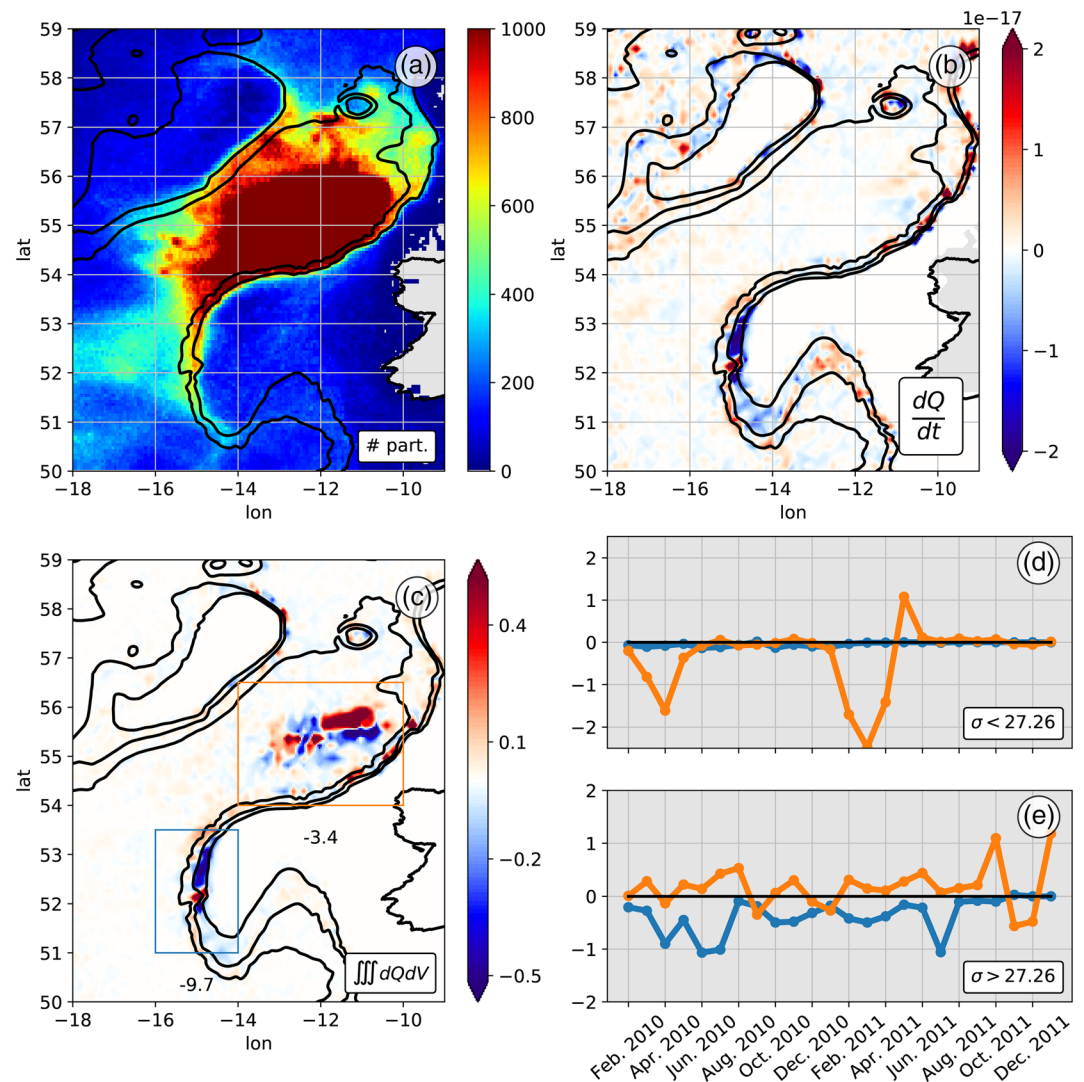
Figure 13. (a) Number of particles present at each location between January 2010 and December 2011, (b) mean PV change, and (c) time and volume-integrated PV change along particle trajectories during the same period. (d, e) Monthly PV change integrated over the two boxes shown in panel (c) for (d) particles lighter than 27.26 kg m^{-3}, and (e) particles denser than 27.26 kg m^{-3}.

and 11h show that the anticyclones generated along the PB transport anomalously salty and warm water that will feed the RT anticyclone during the merger. The time-series and volume-integrated PV changes of particles heavier than 27.3 kg m^{-3} (Figures 13c and 13e) further confirm that the majority of particles merging with the RT anticyclone originate as anticyclonic vortices, generated along the PB slope as a result of current-topography interactions.

The Lagrangian experiment (section 4.2.2) can be used to backtrack the water masses that compose the RT anticyclone at the end of the simulation (December 2011). The T/S properties of the particles inside the RT anticyclone at the seeding time (Figure 12c) show well-mixed waters extending from 27.1 kg m^{-3} at the surface to 27.8 kg m^{-3} at 2,000 m depth. The same is observed in the CTD-derived T/S diagram, based on data along the vertical axis of the RT anticyclone (Figure 5d).

The distributions of particles in the vertical, horizontal, and T/S space 20 months before are shown in Figures 12a–12c. A lot of particles stay trapped in the RT anticyclone, highlighting its coherent structure. Most of the particles entering the RT during this period come from the slope current flowing northward
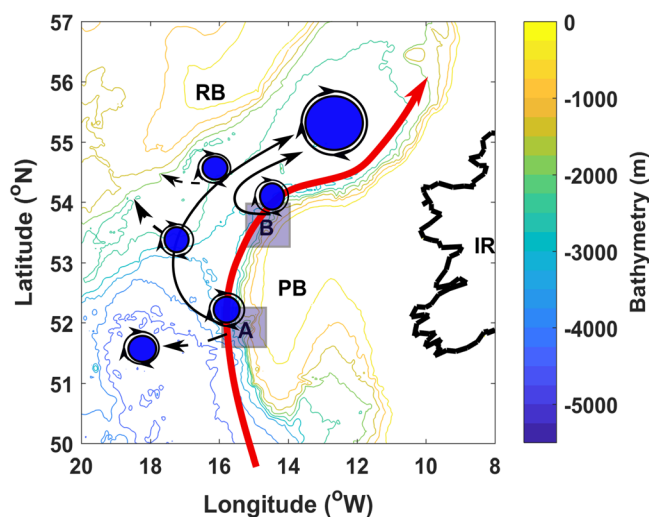
Figure 14. Model-derived schematic representation of the bottom topography-slope current interactions in the southern Rockall Trough (RT), where A and B denote candidate "prime spots" for flow separation due to bottom topography-slope current induced instabilities. Generated small-scale vortices along the east banks of the trough propagate both north-eastward into the trough, thus feeding and sustaining the RT anticyclone, and westward, into the subpolar northeast NA. Letter annotations as in Figure 1.

along the PB, as MOW or ENACW. The density of particles in the T/S space is shown for particles north (Figure 12e) or south of 54°N (Figure 12f). North of 54°N, most of the particles have the same T/S properties as in April 2010, though spreading is visible, in particular for lighter waters in the upper ocean, which extend toward colder and fresher water masses. South of 54°N there are three distinct water masses visible. ENACW fills the upper part of the diagram, above 27.3 kg m^{-3}. A strong mode of MOW is visible below 27.3 kg m^{-3} with high salinity and temperature values. Finally, there is a distinct secondary mode made of SAIW on the same density range but with lower salinity and temperature.

This highlights notable mixing between the different water masses taking place between the southern entrance of the RT (Figure 12f) and the RT anticyclone (Figure 12e). There is presumably isopycnal mixing between SAIW and MOW, along ~27.3–27.6 kg m^{-3} isopycnals, happening during the merger of the smaller anticyclonic vortices with the RT anticyclone. Strong mixing events between ENACW, MOW, and SAIW also occur during the wintertime convective events.

5. Discussion and Conclusions

The presence of a semipermanent anticyclone in the central RT was established in Xu et al. (2015) long-term altimetry study. Using satellite, ship-board, and model data, we show that the altimetry-defined anticyclone is an imprint of a subsurface-intensified anticyclonic vortex, the RT anticyclone, and highlight its vertical structure and formation mechanism.

Satellite and model data confirm the surface signature of the RT anticyclone within 54.5–55.5°N, 12–13°W latitude and longitude respective bands. The ship-board and model data show that the RT anticyclone is a deep vortex, its core delimited by the 27.3–27.7 kg m^{-3} isopycnals, stretching within the ~600/650–1,550 m depth range in the vertical, with a radius of about 40 km. In situ-derived AS, CT, and PV anomalies depict the RT anticyclone's inner core to be located at approximately 1,000 m depth, encompassed within the 27.3/27.4–27.6 kg m^{-3} MOW density ranges.

Our model-based analysis shows that the RT anticyclone is first generated and partly sustained by the merger of smaller scale anticyclones. It does not seem to be the result of a NAC (sub)branch instability, as originally inferred by Xu et al. (2015).

The small-scale anticyclones are generated primarily due to instabilities of the slope current flowing poleward along the eastern RT slope. The generation process follows a sequence of vorticity generation, bottom boundary layer separation, and formation of coherent (sub)mesoscale anticyclones. The anticyclones pinch off at two seemingly prime locations, A and B (Figure 14), as flow transitions between the zonal and meridional slopes of the bank. Some of these small-scale anticyclones merge with the established central RT anticyclone. Vortex merger gives rise to larger structures, and it has been shown to explain the inverse energy cascade (Ciani et al., 2016). Thus, the merging of small-scale anticyclones with the RT anticyclone contributes to its size growth, further to its stability growth, consequently defining the preferential vortex persistency within the vicinity of the region centered at ~55°N, 12°W, which corresponds to the maximum depth of the central RT.

The RT anticyclone is not rigidly attached to a bottom topography feature, which is often the case for quasi-permanent mesoscale vortices in the open ocean (Bashmachnikov et al., 2018). But the variant bottom topography aspect within the vicinity of 55°N, 12°W creates a funnel-like effect, prompting the coalescence of the smaller scale anticyclones and further introducing a topographically induced anchoring of RT anticyclone, once established. The nonstationarity of the anticyclone in the RT could be explained by the presence of cyclones in the interior, known to temporarily alter and deflect anticyclones in proximity (Raj et al., 2015).

Using a barotropic vorticity budget, Le Corre et al. (2019) showed that baroclinic eddy fluxes are the main source of vorticity for the RT anticyclone and that interactions with topography, through bottom pressure

torque and drag, are the main sink of vorticity. This would confirm that the RT anticyclone is intensified by merger with smaller scale anticyclones and controlled by interactions with the bottom topography. The intensification of the RT anticyclone also implies a barotropization of its structure, which results in an intensification of the bottom currents. These currents are responsible for the positive drag curl and positive bottom pressure torque counter-acting the intensification of the RT vortex. The frictional effects resulting from interactions of the RT anticyclone with topography are also observed in the form of an injection of positive vorticity around the anticyclone (Figures 11a–11d).

Our Lagrangian analysis further shows that the main net negative PV contribution to the RT anticyclone comes from the Porcupine slope, where negative PV changes occur due to frictional and diapycnal effects. A second hot-spot for PV transformations is the RT vortex itself, where wintertime convective mixing prompts strong negative PV changes. The deep convection events deepen the mixed-layer, release potential energy by slumping of the isopycnals, and energize the RT anticyclone at depth. The strong convective events are accompanied and followed by positive PV changes, which could be due to several types of submesoscale dynamical instabilities. One is the submesoscale baroclinic instability acting to restratify the mixed-layer at the end of winter and spring (Boccaletti et al., 2007). Another possible candidate would be centrifugal/symmetric instability triggered at the end of winter, prompting a homogenization of PV between the low PV in the core and the high PV in the stratified waters outside of the anticyclone (Kloosterziel et al., 2007). An in-depth modeling analysis of the anticyclone's dynamics is ongoing, to better quantify the mechanisms involved in the RT anticyclone dynamics, and the effects of convection and other possible instabilities on its energetics.

We find that the RT anticyclone shares many characteristics with the Lofoten Basin Eddy (LBE), which is a quasi-permanent anticyclone located in the bathymetric depression of the Lofoten Basin. The generation and sustainment of the LBE are driven by merging events with anticyclones, shed from the eastern branch of the Norwegian Atlantic Current, and by winter convective events (Bashmachnikov et al., 2017; Köhl, 2007; Volkov et al., 2015). In situ observations of the LBE point to the importance of eddy mergers for the heat and salt budgets of the anticyclone (Bosse et al., 2019). Furthermore, PV diagnostics based on the observations also highlight the potential impact of submesoscale instabilities for lateral exchanges between the core and the surroundings (Bosse et al., 2019).

The CTD-based water masses analysis shows that waters forming the core of the RT anticyclone include a large fraction of MOW (50/55–65%), originating primarily from the northward flowing, MOW-rich slope current. This link is supported by the Lagrangian tracking of particles, falling within the regional MOW 27.3–27.7 kg m^{-3} density range.

The RT anticyclone could be viewed as a prime spot for intermediate water masses modifications, with MOW as a primary contributor, as deduced from our water masses fractions analysis and high AHA and ASA estimations. The Lagrangian investigations, confirmed by CTD data from within the anticyclone, show that particles with densities higher than 27.3 kg m^{-3} are predominantly the product of isopycnal/diapycnal mixing between particles with MOW and SAIW characteristics. Exploring the impact of the RT anticyclone on water masses modifications in the region in more details is a next step in our upcoming analyses.

Our model-based deductions on vortices generation along the south-eastern RT slope and their propagation north-eastward into the trough, or westward into the wider subpolar NA, could be direct/indirect heat and salt injections into the Iceland and Irminger basins, and Nordic Seas, inflicting warming up and salinification of upper regional waters from below via mixing. Such eddy-induced fluxes and transports may have an impact for the heat and salt regional and possibly large-scale budgets. This further highlights the importance of the eastern NA boundary dynamics, particularly for the meridional heat and salt transports.

Appendix A: Mixing Triangle Method

The parameterization of the fractions/percentage is based on linear algebra and in that respect, follows the OMP analysis. Data vectors are constructed, where each data point X_i ($i = 1, ..., N$), is represented by a series of M parameter values, X_{ij} ($i = 1, ..., N$, $j = 1, ..., M$), thus compiling a vector X_i (data/sample vector) in M-dimensional parameter space (de Boer & Aken, 1995). Thus, a linear mixing equation, as Equation A.1 with salinity parameter as an example, can be formed for each parameter/variable, in conjunction with

data points/observations at a certain position k; X_1, X_2, X_3 representative of source water masses fractions, AS_1, AS_2, AS_3, representative of AS (g kg^{-1}), and AS (obs) holding the parameter measurement value

$$X_1(k) \times AS_1 + X_2 \times AS_2 + X_3 \times AS_3 = AS \text{ (obs)} \tag{A.1}$$

In matrix form, Equation A.1 could be expressed as follows:

$$X_k \cdot S = Y_k \tag{A.2}$$

where X_k is the ($X_i \times 1$) fractions vector for position k, S is the ($X_j \times X_i$) matrix, holding source water masses characteristics, which is independent of position, and Y_k is the (X_j) vector, holding measurements/observations at position k.

Therefore, as properties of water masses within each triangle represent a mixture between the properties of a respective triangle's water masses, that is, vertices, their respective fractions can thus be solved from linear system of Equation A.3, imposing and including the mass conservation condition for source water mass fractions to sum up to 1 (or 100%), Equation A.4. The linear system of equations to be solved is as follows:

$$
\begin{aligned}
X_1 \times AS_1 + X_2 \times AS_2 + X_3 \times AS_3 &= AS \text{ (obs)} \\
X_1 \times CT_1 + X_2 \times CT_2 + X_3 \times CT_3 &= CT \text{ (obs)}
\end{aligned}
\tag{A.3}
$$

$$
\begin{aligned}
X_1 \times D_1 + X_2 \times D_2 + X_3 \times D_3 &= D \text{ (obs)} \\
X_1 + X_2 + X_3 &= 1 \text{ (or 100\%)}
\end{aligned}
\tag{A.4}
$$

where X_1, X_2, and X_3 (as in Equation A.1) representative of source water masses fractions, AS_1, AS_2, AS_3, CT_1, CT_2, CT_3, D_1, D_2, and D_3 representative of AS (g kg^{-1}), CT (°C), and σ_θ (g m^{-3}) values of source water masses 1, 2, and 3, respectively, allowed to vary within a given range. AS (obs), CT (obs), and D (obs) are values of AS (g kg^{-1}), CT (°C), and σ_θ (kg m^{-3}) of a data point.

In matrix form, for all observations, this could be expressed as **S · X = Y**, where **S** is still representative of the ($X_j \times X_i$) matrix, holding source water masses characteristics, and independent of position, **X** is the ($X_j \times N$) fractions matrix and **Y** is the ($X_j \times N$) measurement matrix.

Generally, the stability of the water column in the vertical is dependent upon density gradient changes, and ultimately, upon the water column temperature and salinity characteristics (Wade et al., 1997). Thus temperature/salinity criteria for data points selection in relation to the domain specified by mixing triangle vertices, that is, water masses, should be sufficient for calculating water masses fractions/percentages. To place the mixing triangle method into an isopycnal framework, and thus to account for processes by which water masses are preserved or transformed across isopycnals (Marsh & Megann, 2002), we incorporated density range criterion within the prerequisites of boundary conditions. This is also performed to add reliability and robustness to the mixing triangle approach adopted here. We run 1,000 random sampling iterations, based on nonparametric bootstrap technique, where the respective source water masses parameters are drawn randomly from observations within their respective AS, CT, and density ranges (for nonparametric approach to resampling, the reader is referred to Thomson & Emery, 2014). The application of random sampling should, in theory, account for the differences in parameters. It should also resolve respective fractions/percentages through the source water matrix variability. As mixing is assumed to occur along straight lines, a source of uncertainty is introduced from the offset of calculations due to the nonlinearity nature of the thermodynamic equation of state. We rectify this partially by including density boundary conditions for each water mass. All parameters boundary conditions (ranges) are provided in Table S4.

Data Availability Statement

CTD data (MI, Ireland) are available upon request (https://www.marine.ie/Home/marine-institute-request-digital-data). Gridded altimeter product details and source are provided within text. Bathymetry data set (NGDC, USA) is available online (http://www.ngdc.noaa.gov/mgg/global/relief/ETOPO2/ETOPO2v2-2006/ETOPO2v2g/). ISAS15 data set (Gaillard et al., 2016; Kolodziejczyk et al., 2017) is available online (https://www.seanoe.org/data/00412/52367). SODA data set (Carton & Giese, 2008) is available online

(https://climatedataguide.ucar.edu/climate-data/soda-simple-ocean-data-assimilation). WOA18 is available online (https://www.nodc.noaa.gov/OC5/woa18/). We thank all filed and scientific teams for the availability of data products. Model sample data are available online (https://github.com/asmilenova/RT_anticyclone_JGR_Oceans).

References

Abernathey, R., & Haller, G. (2018). Transport by Lagrangian vortices in the eastern Pacific. *Journal of Physical Oceanography*, *48*(3), 667–685. https://doi.org/10.1175/JPO-D-17-0102.1

Assassi, C., Morel, Y., Vandermeirsch, F., Chaigneau, A., Pegliasco, C., Morrow, R., et al. (2016). An index to distinguish surface- and subsurface-intensified vortices from surface observations. *Journal of Physical Oceanography*, *46*(8), 2529–2552. https://doi.org/10.1175/JPO-D-15-0122.1

Assene, F., Morel, Y., Delpech, A., Aguedjou, M., Jouanno, J., Cravatte, S., et al. (2020). From mixing to the large scale circulation: How the inverse cascade is involved in the formation of the subsurface currents in the Gulf of Guinea. *Fluids*, *5*(3), 147. https://doi.org/10.3390/fluids5030147

Barceló-Llull, B., Sangrà, P., Pallàs-Sanz, E., Barton, E. D., Estrada-Allis, S. N., Martínez-Marrero, A., et al. (2017). Anatomy of a subtropical intrathermocline eddy. *Deep Sea Research Part I: Oceanographic Research Papers*, *124*, 126–139. https://doi.org/10.1016/j.dsr.2017.03.012

Bashmachnikov, I., Belonenko, T., Kuibin, P., Volkov, D., & Foux, V. (2018). Pattern of vertical velocity in the Lofoten vortex (the Norwegian Sea). *Ocean Dynamics*, *68*(12), 1711–1725. https://doi.org/10.1007/s10236-018-1213-1

Bashmachnikov, I., & Carton, X. (2012). Surface signature of Mediterranean water eddies in the Northeastern Atlantic: Effect of the upper ocean stratification. *Ocean Science*, *8*(6), 931–943. https://doi.org/10.5194/os-8-931-2012

Bashmachnikov, I. L., Sokolovskiy, M. A., Belonenko, T. V., Volkov, D. L., Isachsen, P. E., & Carton, X. (2017). On the vertical structure and stability of the Lofoten vortex in the Norwegian Sea. *Deep Sea Research Part I: Oceanographic Research Papers*, *128*, 1–27. https://doi.org/10.1016/j.dsr.2017.08.001

Boccaletti, G., Ferrari, R., & Fox-Kemper, B. (2007). Mixed layer instabilities and Restratification. *Journal of Physical Oceanography*, *37*(9), 2228–2250. https://doi.org/10.1175/JPO3101.1

Bosse, A., Fer, I., Lilly, J. M., & Søiland, H. (2019). Dynamical controls on the longevity of a non-linear vortex: The case of the Lofoten Basin Eddy. *Scientific Reports*, *9*(1), 13448. https://doi.org/10.1038/s41598-019-49599-8

Bosse, A., Testor, P., Houpert, L., Damien, P., Prieur, L., Hayes, D., et al. (2016). Scales and dynamics of submesoscale coherent vortices formed by deep convection in the northwestern Mediterranean Sea: Vortices in the NW Mediterranean Sea. *Journal of Geophysical Research: Oceans*, *121*, 7716–7742. https://doi.org/10.1002/2016JC012144

Carton, J. A., & Giese, B. S. (2008). A reanalysis of ocean climate using simple ocean data assimilation (SODA). *Monthly Weather Review*, *136*(8), 2999–3017. https://doi.org/10.1175/2007MWR1978.1

Carton, X. (2001). Hydrodynamical modeling of oceanic vortices. *Surveys in Geophysics*, *22*(3), 179–263. https://doi.org/10.1023/A:1013779219578

Chaigneau, A., le Texier, M., Eldin, G., Grados, C., & Pizarro, O. (2011). Vertical structure of mesoscale eddies in the eastern South Pacific Ocean: A composite analysis from altimetry and Argo profiling floats. *Journal of Geophysical Research*, *116*, C11025. https://doi.org/10.1029/2011JC007134

Chelton, D. B., Deszoeke, R. A., Schlax, M. G., Naggar, K. E., & Siwertz, N. (1998). Geographical variability of the first baroclinic Rossby radius of deformation. *Journal of Physical Oceanography*, *28*(3), 433–460. https://doi.org/10.1175/15200485(1998)028<0433:GVOTFB>2.0.CO;2

Chelton, D. B., Schlax, M. G., & Samelson, R. M. (2011). Global observations of nonlinear mesoscale eddies. *Progress in Oceanography*, *91*(2), 167–216. https://doi.org/10.1016/j.pocean.2011.01.002

Chelton, D. B., Schlax, M. G., Samelson, R. M., & de Szoeke, R. A. (2007). Global observations of large oceanic eddies. *Geophysical Research Letters*, *34*, L15606. https://doi.org/10.1029/2007GL030812

Ciani, D., Carton, X., & Verron, J. (2016). On the merger of subsurface isolated vortices. *Geophysical and Astrophysical Fluid Dynamics*, *110*(1), 23–49. https://doi.org/10.1080/03091929.2015.1135430

Courtois, P., Garcia-Quintana, Y., Hu, X., & Myers, P. G. (2020). Kinematic Subduction Rate Of Labrador Sea Water From an Eddy-Permitting Numerical Model. *Journal of Geophysical Research: Oceans*, *125*, e2019JC015475. https://doi.org/10.1029/2019JC015475

D'Asaro, E. A. (1988). Generation of submesoscale vortices: A new mechanism. *Journal of Geophysical Research*, *93*(C6), 6685. https://doi.org/10.1029/JC093iC06p06685

de Boer, C. J., & Aken, H. M. (1995). A study of objective methods for water mass analysis, applied to the Iceland Basin. *Deutsche Hydrographische Zeitschrift*, *47*(1), 5–22. https://doi.org/10.1007/BF02731988

de Boyer Montégut, C. (2004). Mixed layer depth over the global ocean: An examination of profile data and a profile-based climatology. *Journal of Geophysical Research*, *109*, C12003. https://doi.org/10.1029/2004JC002378

de Jong, M. F., van Aken, H. M., Våge, K., & Pickart, R. S. (2012). Convective mixing in the central Irminger Sea: 2002–2010. *Deep Sea Research Part I: Oceanographic Research Papers*, *63*, 36–51. https://doi.org/10.1016/j.dsr.2012.01.003

de Marez, C., Carton, X., L'Hégaret, P., Meunier, T., Stegner, A., Le Vu, B., & Morvan, M. (2020). Oceanic vortex mergers are not isolated but influenced by the β-effect and surrounding eddies. *Scientific Reports*, *10*(1), 2897. https://doi.org/10.1038/s41598-020-59800-y

Debreu, L., Marchesiello, P., Penven, P., & Cambon, G. (2012). Two-way nesting in split-explicit ocean models: Algorithms, implementation and validation. *Ocean Modelling*, *49–50*, 1–21. https://doi.org/10.1016/j.ocemod.2012.03.003

Demirov, E. K., & Pinardi, N. (2007). On the relationship between the water mass pathways and Eddy variability in the Western Mediterranean Sea. *Journal of Geophysical Research*, *112*, C02024. https://doi.org/10.1029/2005JC003174

Ebbesmeyer, C. C., Taft, B. A., Mcwilliams, J. C., Shen, C. Y., Riser, S. C., Rossby, H. T., et al. (1986). Detection, structure, and origin of extreme anomalies in a Western Atlantic oceanographic section. *Journal of Physical Oceanography*, *16*(3), 591–612. https://doi.org/10.1175/1520-0485(1986)016<0591:DSAOOE>2.0.CO;2

Ellett, D., Edwards, A., & Bowers, R. (1986). The hydrography of the Rockall Channel—An overview. *Proceedings of the Royal Society of Edinburgh*, *88B*, 61–81.

Feucher, C., Maze, G., & Mercier, H. (2016). Mean structure of the North Atlantic subtropical permanent pycnocline from in situ observations. *Journal of Atmospheric and Oceanic Technology*, *33*(6), 1285–1308. https://doi.org/10.1175/JTECH-D-15-0192.1

Fischer, J., Karstensen, J., Oltmanns, M., & Schmidtko, S. (2018). Mean circulation and EKE distribution in the Labrador sea water level of the subpolar North Atlantic. *Ocean Science Discussions*, 1–27. https://doi.org/10.5194/os-2018-56

Flierl, G. R. (1981). Particle motions in large-amplitude wave fields. *Geophysical and Astrophysical Fluid Dynamics*, *18*(1–2), 39–74. https://doi.org/10.1080/03091928108208773

Fomin, L. M. (1964). *The dynamic method in oceanography*. Burlington: Elsevier. ISBN 9780444402400

Frenger, I., Bianchi, D., Stührenberg, C., Oschlies, A., Dunne, J., Deutsch, C., et al. (2018). Biogeochemical role of subsurface coherent eddies in the ocean: Tracer cannonballs, hypoxic storms, and microbial stewpots? *Global Biogeochemical Cycles*, *32*, 226–249. https://doi.org/10.1002/2017GB005743

Gaillard, F., Reynaud, T., Thierry, V., Kolodziejczyk, N., & von Schuckmann, K. (2016). In-situ based reanalysis of the global ocean temperature and salinity with ISAS: Variability of the heat content and steric height. *Journal of Climate*, *29*(4), 1305–1323. Publisher's official version. https://doi.org/10.1175/JCLI-D-15-0028.1, open access version, https://archimer.ifremer.fr/doc/00309/42030/

Garcia-Quintana, Y., Courtois, P., Hu, X., Pennelly, C., Kieke, D., & Myers, P. G. (2019). Sensitivity of Labrador sea water formation to changes in model resolution, atmospheric forcing, and freshwater input. *Journal of Geophysical Research: Oceans*, *124*, 2126–2152. https://doi.org/10.1029/2018JC014459

Graham, J. A., Rosser, J. P., O'Dea, E., & Hewitt, H. T. (2018). Resolving shelf break exchange around the European northwest shelf. *Geophysical Research Letters*, *45*, 12,386–12,395. https://doi.org/10.1029/2018GL079399

Griffiths, R., & Hopfinger, E. (1987). Coalescing of geostrophic vortices. *Journal of Fluid Mechanics*, *178*, 73–97. https://doi.org/10.1017/S0022112087001125

Gula, J., Blacic, T. M., & Todd, R. E. (2019). Submesoscale coherent vortices in the Gulf stream. *Geophysical Research Letters*, *46*, 2704–2714. https://doi.org/10.1029/2019GL081919

Gula, J., Molemaker, M. J., & McWilliams, J. C. (2014). Submesoscale cold filaments in the Gulf stream. *Journal of Physical Oceanography*, *44*(10), 2617–2643. https://doi.org/10.1175/JPO-D-14-0029.1

Gula, J., Molemaker, M. J., & McWilliams, J. C. (2015). Topographic vorticity generation, submesoscale instability and vortex street formation in the Gulf stream. *Geophysical Research Letters*, *42*, 4054–4062. https://doi.org/10.1002/2015GL063731

Gula, J., Molemaker, M. J., & McWilliams, J. C. (2016a). Submesoscale dynamics of a gulf stream frontal Eddy in the South Atlantic bight. *Journal of Physical Oceanography*, *46*(1), 305–325. https://doi.org/10.1175/JPO-D-14-0258.1

Gula, J., Molemaker, M. J., & McWilliams, J. C. (2016b). Topographic generation of submesoscale centrifugal instability and energy dissipation. *Nature Communications*, *7*(1), 12811. https://doi.org/10.1038/ncomms12811

Halo, I., Backeberg, B., Penven, P., Ansorge, I., Reason, C., & Ullgren, J. E. (2014). Eddy properties in the Mozambique channel: A comparison between observations and two numerical ocean circulation models. *Deep Sea Research Part II: Topical Studies in Oceanography*, *100*, 38–53. https://doi.org/10.1016/j.dsr2.2013.10.015

Halo, I., Penven, P., Backeberg, B., Ansorge, I., Shillington, F., & Roman, R. (2014). Mesoscale eddy variability in the southern extension of the East Madagascar current: Seasonal cycle, energy conversion terms, and eddy mean properties. *Journal of Geophysical Research: Oceans*, *119*, 7324–7356. https://doi.org/10.1002/2014JC009820

Haynes, P. H., & McIntyre, M. E. (1987). On the evolution of vorticity and potential vorticity in the presence of diabatic heating and frictional or other forces. *Journal of the Atmospheric Sciences*, *44*(5), 828–841. https://doi.org/10.1175/1520-0469(1987)044h0828:OTEOVAi2.0.CO;2

Heywood, K. J., McDonagh, E. L., & White, M. A. (1994). Eddy kinetic energy of the North Atlantic subpolar gyre from satellite altimetry. *Journal of Geophysical Research*, *99*(C11), 22525. https://doi.org/10.1029/94JC01740

Holliday, N. P., Cunningham, S. A., Johnson, C., Gary, S. F., Griffiths, C., Read, J. F., & Sherwin, T. (2015). Multidecadal variability of potential temperature, salinity, and transport in the eastern subpolar North Atlantic: Variability in subpolar N. Atlantic. *Journal of Geophysical Research: Oceans*, *120*, 5945–5967. https://doi.org/10.1002/2015JC010762

Houpert, L., Inall, M. E., Dumont, E., Gary, S., Johnson, C., Porter, M., et al. (2018). Structure and transport of the North Atlantic current in the eastern subpolar gyre from sustained glider observations: Obs. transport nac. *Journal of Geophysical Research: Oceans*, *123*, 6019–6038. https://doi.org/10.1029/2018JC014162

IOC, SCOR, and IAPSO (2010). The International Thermodynamic Equation of Seawater—2010: Calculation and use of thermodynamic properties. Intergovernmental Oceanographic Commission, Manuals and Guides. UNESCO (English), [Available at: http://www.teos-10.org]

Isern-Fontanet, J., García-Ladona, E., & Font, J. (2006). Vortices of the Mediterranean Sea: An altimetric perspective. *Journal of Physical Oceanography*, *36*(1), 87–103. https://doi.org/10.1175/JPO2826.1

Karstensen, J., & Tomczak, M. (1998). Age determination of mixed water masses using CFC and oxygen data. *Journal of Geophysical Research*, *103*(C9), 18,599–18,609. https://doi.org/10.1029/98JC00889

Kloosterziel, R. C., Carnevale, G. F., & Orlandi, P. (2007). Inertial instability in rotating and stratified fluids: Barotropic vortices. *Journal of Fluid Mechanics*, *583*, 379–412. https://doi.org/10.1017/S0022112007006325

Köhl, A. (2007). Generation and stability of a quasi-permanent vortex in the Lofoten basin. *Journal of Physical Oceanography*, *37*(11), 2637–2651. https://doi.org/10.1175/2007JPO3694.1

Kolodziejczyk, N., Prigent-Mazella, A., & Gaillard, F. (2017). ISAS-15 temperature and salinity gridded fields. SEANOE. https://doi.org/10.17882/52367

Langehaug, H. R., & Falck, E. (2012). Changes in the properties and distribution of the intermediate and deep waters in the Fram Strait. *Progress in Oceanography*, *96*(1), 57–76. https://doi.org/10.1016/j.pocean.2011.10.002

Laxenaire, R., Speich, S., Blanke, B., Chaigneau, A., Pegliasco, C., & Stegner, A. (2018). Anticyclonic eddies connecting the western boundaries of Indian and Atlantic oceans. *Journal of Geophysical Research: Oceans*, *123*, 7651–7677. https://doi.org/10.1029/2018JC014270

Le Corre, M., Gula, J., Smilenova, A., & Houpert, L. (2019). On the dynamics of a deep quasi-permanent anticyclonic Eddy in the Rockall Trough, 24ème Congrès Français de Mécanique, Brest, France

Le Corre, M., Gula, J., & Treguier, A.-M. (2020). Barotropic vorticity balance of the North Atlantic subpolar gyre in an Eddy-resolving model. *Ocean Science*, *16*(2), 451–468. https://doi.org/10.5194/os-16-451-2020

Le Vu, B., Stegner, A., & Arsouze, T. (2018). Angular momentum Eddy detection and tracking algorithm (AMEDA) and its application to coastal Eddy formation. *Journal of Atmospheric and Oceanic Technology*, *35*(4), 739–762. https://doi.org/10.1175/JTECH-D-17-0010.1

Lorenz, E. N. (1955). Available potential energy and the maintenance of the general circulation. *Tellus*, *7*(2), 157–167. https://doi.org/10.1111/j.2153-3490.1955.tb01148.x

Lozier, M. S. (1997). Evidence for large-scale Eddy-driven gyres in the North Atlantic. *Science*, *277*(5324), 361–364. https://doi.org/10.1126/science.277.5324.361

Mamayev, O. I. (1975). *Temperature-salinity analysis of world ocean waters* (Vol. 11). New York: Elsevier science. ebook ISBN: 9780080870472

Marchesiello, P., Benshila, R., Almar, R., Uchiyama, Y., McWilliams, J. C., & Shchepetkin, A. (2015). On tridimensional rip current modeling. *Ocean Modelling*, *96*, 36–48. https://doi.org/10.1016/j.ocemod.2015.07.003

Marnela, M., Rudels, B., Goszczko, I., Beszczynska-Möller, A., & Schauer, U. (2016). Fram Strait and Greenland Sea transports, water masses, and water mass transformations 1999–2010 (and beyond): Fram Strait and Greenland Sea transports. *Journal of Geophysical Research: Oceans*, *121*, 2314–2346. https://doi.org/10.1002/2015JC011312

Marsh, R., Haigh, I. D., Cunningham, S. A., Inall, M. E., Porter, M., & Moat, B. I. (2017). Large-scale forcing of the European slope current and associated inflows to the North Sea. *Ocean Science*, *13*(2), 315–335. https://doi.org/10.5194/os-13-315-2017

Marsh, R., & Megann, A. P. (2002). Tracing water masses with particle trajectories in an isopycnic-coordinate model of the global ocean. *Ocean Modelling*, *4*(1), 27–53. https://doi.org/10.1016/S1463-5003(01)00011-7

Marshall, J., Jamous, D., & Nilsson, J. (2001). Entry, flux, and exit of potential vorticity in ocean circulation. *Journal of Physical Oceanography*, *31*(3), 777–789. https://doi.org/10.1175/1520-0485(2001)031<0777:EFAEOP>2.0.CO;2

McDougall, T. J., & Barker, P. M. (2011). Getting started with TEOS-10 and the Gibbs seawater (GSW) oceanographic toolbox, 28 pp., SCOR/IAPSO WG127, ISBN 978-0-646-55621-5

McGrath, T., Nolan, G., & McGovern, E. (2012). Chemical characteristics of water masses in the Rockall trough. *Deep Sea Research Part I: Oceanographic Research Papers*, *61*, 57–73. https://doi.org/10.1016/j.dsr.2011.11.007

McWilliams, J. C. (1985). Submesoscale, coherent vortices in the ocean. *Reviews of Geophysics*, *23*(2), 165. https://doi.org/10.1029/RG023i002p00165

Molemaker, M. J., McWilliams, J. C., & Dewar, W. K. (2015). Submesoscale instability and generation of Mesoscale anticyclones near a separation of the California undercurrent. *Journal of Physical Oceanography*, *45*(3), 613–629. https://doi.org/10.1175/JPO-D-13-0225.1

Morel, Y., Gula, J., & Ponte, A. (2019). Potential vorticity diagnostics based on balances between volume integral and boundary conditions. *Ocean Modelling*, *138*, 23–35. https://doi.org/10.1016/j.ocemod.2019.04.004

Morel, Y., & McWilliams, J. (1997a). Evolution of isolated interior vortices in the ocean. *Journal of Physical Oceanography*, *27*(5), 727–748. https://doi.org/10.1175/15200485(1997)027<0727:EOIIVI>2.0.CO;2

Morrow, R., & Birol, F. (2004). Divergent pathways of cyclonic and anticyclonic ocean eddies. *Geophysical Research Letters*, *31*, L24311. https://doi.org/10.1029/2004GL020974

Mosquera Giménez, Á., Vélez-Belchí, P., Rivera, J., Piñeiro, S., Fajar, N., Caínzos, V., et al. (2019). Ocean circulation over North Atlantic underwater features in the path of the Mediterranean outflow water: The Ormonde and Formigas seamounts, and the Gazul mud volcano. *Frontiers in Marine Science*, *6*, 702. https://doi.org/10.3389/fmars.2019.00702

Naylor, D., Shannon, P., & Murphy, N. (1999). Irish Rockall Basin region: A standard structural nomenclature system. Petroleum affairs div., Dept. of the marine and natural resources, Dublin, ISBN 0-7076-6289-3

New, A. L., Barnard, S., Herrmann, P., & Molines, J.-M. (2001). On the origin and pathway of the saline inflow to the Nordic seas: Insights from models. *Progress in Oceanography*, *48*(2–3), 255–287. https://doi.org/10.1016/S0079-6611(01)00007-6

Okubo, A. (1970). Horizontal dispersion of floatable particles in the vicinity of velocity singularities such as convergences. *Deep Sea Research and Oceanographic Abstracts*, *17*(3), 445–454. https://doi.org/10.1016/0011-7471(70)90059-8

Penven, P., Debreu, L., Marchesiello, P., & McWilliams, J. C. (2006). Evaluation and application of the ROMS 1-way embedding procedure to the Central California upwelling system. *Ocean Modelling*, *12*(1–2), 157–187. https://doi.org/10.1016/j.ocemod.2005.05.002

Petersen, M. R., Williams, S. J., Maltrud, M. E., Hecht, M. W., & Hamann, B. (2013). A three-dimensional eddy census of a high-resolution GLOBAL ocean simulation: 3-D global Eddy census. *Journal of Geophysical Research: Oceans*, *118*, 1759–1774. https://doi.org/10.1002/jgrc.20155

Pujol, M.-I., Faugère, Y., Taburet, G., Dupuy, S., Pelloquin, C., Ablain, M., & Picot, N. (2016). DUACS DT2014: The new multi-mission altimeter data set reprocessed over 20 years. *Ocean Science*, *12*(5), 1067–1090. https://doi.org/10.5194/os-12-1067-2016

Raj, R. P., Chafik, L., Nilsen, J. E. Ø., Eldevik, T., & Halo, I. (2015). The Lofoten vortex of the Nordic seas. *Deep Sea Research Part I: Oceanographic Research Papers*, *96*, 1–14. https://doi.org/10.1016/j.dsr.2014.10.011

Renault, L., Molemaker, M. J., McWilliams, J. C., Shchepetkin, A. F., Lemarié, F., Chelton, D., et al. (2016). Modulation of Wind Work by Oceanic Current Interaction with the Atmosphere. *Journal of Physical Oceanography*, *46*(6), 1685–1704. https://doi.org/10.1175/jpo-d-15-0232.1

Roullet, G., Capet, X., & Maze, G. (2014). Global interior eddy available potential energy diagnosed from Argo floats. *Geophysical Research Letters*, *41*, 1651–1656. https://doi.org/10.1002/2013GL059004

Sandwell, D. T., & Smith, W. H. F. (1997). Marine gravity anomaly from Geosat and ERS 1 satellite altimetry. *Journal of Geophysical Research*, *102*(B5), 10,039–10,054. https://doi.org/10.1029/96JB03223

Schubert, R., Gula, J., Greatbatch, R. J., Baschek, B., & Biastoch, A. (2020). The submesoscale kinetic energy cascade: Mesoscale absorption of submesoscale mixed layer eddies and frontal downscale fluxes. *Journal of Physical Oceanography*, *50*(9), 2573–2589. https://doi.org/10.1175/JPO-D-19-0311.1

Shchepetkin, A. F., & McWilliams, J. C. (2005). The regional oceanic modeling system (ROMS): A split-explicit, free-surface, topography-following-coordinate oceanic model. *Ocean Modelling*, *9*(4), 347–404. https://doi.org/10.1016/j.ocemod.2004.08.002

Srinivasan, K., McWilliams, J. C., Molemaker, M. J., & Barkan, R. (2019). Submesoscale vortical wakes in the lee of topography. *Journal of Physical Oceanography*, *49*(7), 1949–1971. https://doi.org/10.1175/JPO-D-18-0042.1

Testor, P., Bosse, A., Houpert, L., Margirier, F., Mortier, L., Legoff, H., et al. (2018). Multiscale observations of DEEP convection in the Northwestern Mediterranean Sea during winter 2012–2013 using multiple platforms: Multiscale deep convection observations. *Journal of Geophysical Research: Oceans*, *123*, 1745–1776. https://doi.org/10.1002/2016JC012671

Thomson, R., & Emery, W. (2014). *Data analysis methods in physical oceanography*. New York: Elsevier Science. ISBN 9780123877826

Treguier, A. M., Deshayes, J., Lique, C., Dussin, R., & Molines, J. M. (2012). Eddy contributions to the meridional transport of salt in the North Atlantic. *Journal of Geophysical Research*, *117*, C05010. https://doi.org/10.1029/2012JC007927

Umlauf, L., & Burchard, H. (2003). A generic length-scale equation for geophysical turbulence models. *Journal of Marine Research*, *61*(2), 235–265. https://doi.org/10.1357/002224003322005087

Vic, C., Gula, J., Roullet, G., & Pradillon, F. (2018). Dispersion of deep-sea hydrothermal vent effluents and larvae by submesoscale and tidal currents. *Deep Sea Research Part I: Oceanographic Research Papers*, *133*, 1–18. https://doi.org/10.1016/j.dsr.2018.01.001

Vic, C., Roullet, G., Capet, X., Carton, X., Molemaker, M. J., & Gula, J. (2015). Eddy-topography interactions and the fate of the Persian Gulf Outflow. *Journal of Geophysical Research: Oceans*, *120*, 6700–6717. https://doi.org/10.1002/2015JC011033

Volkov, D. L. (2005). Interannual variability of the altimetry-derived Eddy field and surface circulation in the Extratropical North Atlantic Ocean in 1993–2001. *Journal of Physical Oceanography*, *35*(4), 405–426. https://doi.org/10.1175/JPO2683.1

Volkov, D. L., Kubryakov, A. A., & Lumpkin, R. (2015). Formation and variability of the Lofoten basin vortex in a high-resolution ocean model. *Deep Sea Research Part I: Oceanographic Research Papers*, *105*, 142–157. https://doi.org/10.1016/j.dsr.2015.09.001

Vortmeyer-Kley, R., Gräwe, U., & Feudel, U. (2016). Detecting and tracking eddies in oceanic flow fields: A Lagrangian descriptor based on the modulus of vorticity. *Nonlinear Processes in Geophysics*, *23*(4), 159–173. https://doi.org/10.5194/npg-23-159-2016

Wade, I. P., Ellett, D. J., & Heywood, K. J. (1997). The influence of intermediate waters on the stability of the eastern North Atlantic. *Deep Sea Research Part I: Oceanographic Research Papers*, *44*(8), 1405–1426. https://doi.org/10.1016/S0967-0637(97)00023-X

Weiss, J. (1991). The dynamics of enstrophy transfer in two-dimensional hydrodynamics. *Physica D: Nonlinear Phenomena*, *48*(2–3), 273–294. https://doi.org/10.1016/0167-2789(91)90088-Q

White, M. A., & Heywood, K. J. (1995). Seasonal and interannual changes in the North Atlantic subpolar gyre from Geosat and TOPEX/ POSEIDON altimetry. *Journal of Geophysical Research*, *100*(C12), 24931. https://doi.org/10.1029/95JC02123

Xu, W., Miller, P. I., Quartly, G. D., & Pingree, R. D. (2015). Seasonality and interannual variability of the European slope current from 20 years of altimeter data compared with in situ measurements. *Remote Sensing of Environment*, *162*, 196–207. https://doi.org/10.1016/j.rse.2015.02.008

Zhang, Z., Wang, W., & Qiu, B. (2014). Oceanic mass transport by mesoscale eddies. *Science*, *345*(6194), 322–324. https://doi.org/10.1126/science.1252418

Zhao, J., Bower, A., Yang, J., & Lin, X. (2018). Meridional heat transport variability induced by mesoscale processes in the subpolar North Atlantic. *Nature Communications*, *9*(1), 1–9. https://doi.org/10.1038/s41467-018-03134-x

Zhao, J., Bower, A., Yang, J., Lin, X., & Zhou, C. (2018). Structure and formation of Anticyclonic eddies in the Iceland Basin. *Journal of Geophysical Research: Oceans*, *123*, 5341–5359. https://doi.org/10.1029/2018JC013886